

Multidimensional Radiation Hydrodynamics Simulations of Supernova 1987A Shock Breakout

WUN-YI CHEN,^{1,2} KE-JUNG CHEN,¹ AND MASAOMI ONO^{1,3}

¹*Institute of Astronomy and Astrophysics, Academia Sinica, Taipei 10617, Taiwan*

²*National Taiwan University, Graduate Institute of Astrophysics*

*Department of Physics/Center for Condensed Building R401, No.1, Sec. 4, Roosevelt Rd,
Taipei 10617, Taiwan*

³*Astrophysical Big Bang Laboratory (ABBL), RIKEN Cluster for Pioneering Research,
2-1 Hirosawa, Wako, Saitama 351-0198, Japan*

ABSTRACT

Shock breakout is the first electromagnetic signal from supernovae (SNe), which contains important information on the explosion energy and the size and chemical composition of the progenitor star. This paper presents the first two-dimensional (2D) multi-wavelength radiation hydrodynamics simulations of SN 1987A shock breakout by using the **CASTRO** code with the opacity table, **OPAL**, considering eight photon groups from infrared to X-ray. To investigate the impact of the pre-supernova environment of SN 1987A, we consider possible three cases of circumstellar medium (CSM) environments: only a steady wind; an eruptive mass loss; and the existence of a companion star. In sum, the resulting breakout light curve has an hour duration and its peak luminosity of $\sim 6 \times 10^{46} \text{ erg s}^{-1}$ following efficient post-breakout X-ray cooling of $\sim 3.5 \text{ mag hour}^{-1}$. The dominant band transits to UV after around 3 hours of shock breakout and its luminosity has a decay rate of $\sim 1.5 \text{ mag hour}^{-1}$ that agrees well with the observed shock breakout tail. The detailed features of breakout emission are sensitive to the pre-explosion environment. Our 2D simulations also demonstrate the importance of post-breakout mixing and its impacts on shock dynamics and radiation emission. The mixing driven by the shock breakout may lead to a global asymmetry of SN ejecta and affect its later supernova remnant formation.

Keywords: Supernovae — Ultraviolet astronomy — Radiation hydrodynamics

1. INTRODUCTION

The electromagnetic signals from supernovae (SNe) of massive stars begin when the explosion shock breaks out of the stellar surface. This is the so-called *shock breakout*, a luminous phenomenon that has only been detected through a few serendipitous observations (Schawinski et al. 2008; Gezari et al. 2015). The peak luminosity and duration of breakout emission can be used to probe the explosion energy, the radius of a progenitor star, and its circumstellar environment (Waxman & Katz 2017).

Previous theoretical studies of shock breakout duration and peak luminosity from blue supergiant (BSG) and red supergiant (RSG) usually assumed an adiabatic shock propagating in a spherical stellar envelope with a power-law density profile (Matzner & McKee 1999; Waxman & Katz 2017). However, modeling the realistic SN shock breakout requires a deeper understanding of the shock propagation in a clumpy stellar atmosphere and the circumstellar medium (CSM) formed before the star dies (Chevalier & Irwin 2011; González-Torà, G. et al. 2023), and the emission from the shock typically ranges from hard X-ray to UV and infrared wavelengths (Tolstov et al. 2013; Katz et al. 2010). The complex interplay of radiation-mediated shock among the structured stellar atmosphere and CSM can only be properly modeled through the multidimensional radiation hydrodynamics (RHD) (Levinson & Nakar 2020), which has been utilized to model the transport of neutrinos and photons in supernovae (Ott et al. 2008; Utrobin et al. 2021; Chen et al. 2023).

Previous one-dimensional (1D) shock breakout simulations (Lovegrove et al. 2017) have provided insights into the physics of SN shock breakout. However, these simulations have limitations, as they fail to accurately model fluid instabilities, resulting in nonphysical features such as a distinct density spike (thin shell). Limited fluid instabilities in 1D simulations often concentrate a significant amount of shocked ejecta into a small region, moving at the same

velocity, and lead to the formation of a nonphysical thin shell. This thin shell, where most of the electromagnetic emission originates, may underestimate the peak luminosity and the duration of the breakout emission. Furthermore, 2D hydrodynamics shock breakouts by Couch et al. (2011) revealed a longer shock breakout duration and locally higher peak luminosity due to more efficient mixing in 2D. Therefore, the difference between the 1D and 2D RHD simulation of the shock breakout is essential.

2D frequency-integrated RHD simulations of shock breakout (Suzuki et al. 2016; Suzuki & Maeda 2021) have revealed the emergence of bipolar explosion shocks on the stellar surface as a possible source of long-lived bright emission. 3D RHD simulations on red supergiant (RSG) envelopes have also shown density fluctuations in the stellar surface may extend the shock breakout duration (Goldberg et al. 2022).

However, these simulations, only containing a single energy group of photon (known as *grey* approximation), fail to capture the shock heating and cooling processes that generate X-ray and UV emissions, accurately. The corresponding grey opacity falls short in producing a cooling shell during the free expansion phase of the ejecta. To investigate the shock breakout, one has to follow the propagation of the forward shock into regions from optically thin to optically thick regions, i.e., from low to high Mach numbers, as well as its interaction with CSM to drive the post-shocked mixing. Therefore, 2D shock breakout RHD simulations, combined with multi-group radiation transport spanning hard X-rays to near-infrared radiation, are indispensable. This paper presents the first results of multidimensional multi-group RHD simulations of SN shock breakout, modeling more realistic SN shock breakout emissions.

To conduct simulations incorporating CSM alterations and facilitating comparisons with 1D calculations, we employ 2D Multi-Group Flux Limited Diffusion (MGFLD) in CASTRO (Almgren et al. 2020; Almgren et al. 2010), utilizing OPAL opacity tables (Iglesias & Rogers 1996).

We use SN models for SN 1987A for our shock breakout study. SN 1987A stands out among well-studied supernova targets. With plenty of observations and detailed investigations, including shock breakout estimations (Ensmann & Burrows 1992; Imshennik & Nadezhin 1988; Lovegrove et al. 2017), SN 1987A makes itself an ideal candidate for probing multi-dimensional supernova shock breakout phenomena.

The progenitor star of SN 1987A has been known as a compact BSG (Walborn et al. 1987; West et al. 1987) with a radius of $(2-4) \times 10^{12}$ cm (Arnett et al. 1989). Recent theoretical studies (Menon et al. 2019; Ono et al. 2020; Orlando et al. 2020; Utrobin et al. 2021) with progenitor models based on a binary merger scenario for SN 1987A (Menon & Heger 2017; Urushibata et al. 2018) have overall supported this scenario including modeling of LCs after the shock breakout (Menon et al. 2019; Utrobin et al. 2021). Several related studies on SN 1987A with the binary merger progenitor models have also been reported (Alp et al. 2019; Greco et al. 2021, 2022; Nakamura et al. 2022; Dohi et al. 2023; Ono et al. 2023; Sapienza et al. 2024).

We conduct simulations to calculate luminosity variation curves (LCs) by considering different wavelength bands and viewing angles for SN 1987A (see Table 1 for details). Although recent studies have shown the binary merger progenitors better describe the optical (Menon et al. 2019; Utrobin et al. 2021) and X-ray (Orlando et al. 2020) LCs as partly mentioned, to compare our results with those of the previous study (Lovegrove et al. 2017), we adopt the same $15 M_{\odot}$ single star progenitor (a BSG) for SN 1987A and are motivated by the asymmetries in the nebula of SN 1987A (e.g. Sugerman et al. 2005) to incorporate inhomogeneity in stellar envelopes and CSM, including perturbations, a ring-like structure caused by an eruptive mass loss, and a binary companion star (Tsai et al. 2023) to investigate the impact of variety of CSM environments. Furthermore, we explore the CSM profiles resulting from a steady stellar wind of varying strengths, spanning two orders of magnitude.

We introduce the CASTRO code, progenitor models, and methodologies in § 2. We examine the effects of resolution and perturbation amplitudes on the shock and verify the necessity of RHD in § 3. Our simulation results are presented in § 4, § 5, and § 6. The significance and implications of our work are discussed in § 7. Finally, we conclude our findings in § 8.

2. NUMERICAL METHOD

2.1. CASTRO

CASTRO (Almgren et al. 2020; Almgren et al. 2010) is a compressible RHD code that solves hyperbolic radiation fluid and frequency space advection with the higher-order Godunov scheme and solves photon diffusion and source-sink terms by first-order backward Euler method. It uses co-moving frame Multi-Group Flux Limited Diffusion approximation (MGFLD) RHD (Zhang et al. 2011, 2013) with Poisson gravity (Katz et al. 2016). CASTRO is equipped with highly parallel Adaptive Mesh Refinement (AMR) to resolve turbulent fine structures formed in explosive phenomena.

We perform 2D simulations of the shock breakout using the cylindrical coordinates $(r - z)$ covering direction angles $\theta = 0 - 90$ and $\phi = 0 - 360$ degrees with a symmetry along z , which essentially represents an axisymmetric half-sphere of the shock breakout. The lower and upper boundaries of the r and z axes are set as reflective and outflow boundaries, respectively. Our simulations are conducted in a box with the size of 10^{14} cm \times 10^{14} cm for the 2D single star SN 1987A simulations, employing a resolution of 1024^2 . For simulations of an explosion with a nearby companion star, we use a box with the size of 4×10^{13} cm \times 4×10^{13} cm with a higher grid resolution of 2048^2 in Cartesian coordinates. Single simulation with 1024^2 resolution, 8 groups MGFLD, and OPAL opacity takes around a thousand CPU hours on the Kawas Cluster at ASIAA.

2.1.1. Gas Physics

We adopt a γ law equation of state for the shock breakout problem due to the wide range of gas density (10^{-15} g cm $^{-3}$ to 10^{-3} g cm $^{-3}$) and temperature (10^4 K to 10^7 K) in our simulations. The ideal gas with $\gamma = 5/3$ is appropriate for this density and temperature range. As our simulations commence after the cessation of explosive nucleosynthesis, nuclear reaction networks are omitted.

2.1.2. Radiation Hydrodynamics

The RHD module of CASTRO (Zhang et al. 2011) independently evolves the temperatures of gas and radiation. The introduction of radiation cooling and heating terms is represented by $\partial_t E_{\text{gas}} \propto c(aT^4 - E_r)$, which captures the balance between the gas energy E_{gas} and radiation energy E_r . This equation characterizes the local radiative heating and cooling process. As the shock propagates, the radiation temperature and gas temperature of a cell can vary, allowing for a non-thermalized radiation spectrum.

CASTRO MGFLD module (Zhang et al. 2013) enables multi-group radiation transport and can evaluate the color evolution of shock breakout. Furthermore, radiation precursors caused by the shock interaction with the CSM also heat up the pre-shocked regions. CASTRO MGFLD employs a closure relation and flux approximate limiter between the radiation flux and the radiation energy to ensure isotropic diffusion in optically thick regions and that in the free streaming region, the radiation flux adopts the form $\|F_r\| = cE_r$, where F_r represents the radiation flux, E_r is the radiation energy, and c denotes the speed of light. FLD approximation aligns effectively with the shock breakout scenario, where radiation flux follows non-unidirectional paths relative to the velocity vector, depending on the breakout environments.

In our 2D simulations, we consider photon frequencies ranging from 10^{13} Hz to 10^{19} Hz, dividing them into 8 groups with a logarithmic scale spacing. These resulting photon groups span from mid-infrared to X-rays. The specific range of each group is outlined in Table 1. At the simulation's outset, the radiation energy of each cell is set to $E_r = aT^4$, where a represents the radiation constant. This value is based on the gas temperature T from the progenitor stars, assuming local thermal equilibrium.

We calculate the LCs by tallying the photons passing through the virtual observer point close to the boundary of the simulation box. The luminosity of the breakout can be expressed as

$$L(\nu, \theta) = 4\pi r_s^2 \times F_{\nu, r}, \quad (1)$$

where $L(\nu, \theta)$ is the luminosity in frequency band entered ν at different viewing angles θ . $r_s = 8 \times 10^{13}$ cm is the radius of the fixed observer point from the center of the progenitor star, and $F_{\nu, r}$ is the corresponding radiation flux.

2.1.3. Opacity

We adopt opacity from OPAL table (Iglesias & Rogers 1996). Instead of approximating constant opacity, OPAL can better model the total opacity in the shock cooling shell and the regions with turbulent structures. OPAL takes the inputs of the gas density, electron density, hydrogen fraction, helium fraction, metallicity, and temperature from the gas in each cell and yields the opacity for each photon group. In our simulations, we only consider the envelope region, which contains mainly hydrogen and helium and a tiny fraction of heavy elements. Therefore, we do not consider the opacity contributed by individual heavy elements. Assuming the gas is fully ionized, we adopt the hydrogen fraction, helium fraction, and metallicity ¹ as $X = 0.47$, $Y = 0.52$, and $Z \sim 0.01$, respectively. It is noted that the differences

¹ Note: the values of the binary merger progenitor model (Urushibata et al. 2018) of 1987A, adopted e.g., in the previous studies (Ono et al. 2020; Orlando et al. 2020), are $X = 0.639$; $Y = 0.355$; $Z = 0.006$.

Table 1. Radiation Groups

Band	Central Frequency (Hz)	Band Width (Hz)	Central Wavelength (Å)
(1)	(2)	(3)	(4)
I	2.37×10^{13}	4.62×10^{13}	1.26×10^5
II	1.33×10^{14}	2.59×10^{14}	2.25×10^4
III	7.49×10^{14}	1.46×10^{15}	4.00×10^3
IV	4.21×10^{15}	8.22×10^{15}	7.12×10^2
V	2.37×10^{16}	4.62×10^{16}	1.26×10^2
VI	1.33×10^{17}	2.59×10^{17}	2.25×10
VII	7.49×10^{17}	1.46×10^{18}	4.00
VIII	4.21×10^{18}	8.22×10^{18}	7.12×10^{-1}

NOTE—The table shows the eight bands I–VIII of radiation groups. Information for each group contains the central frequency, bandwidth, and central wavelength.

in the metallicity by a factor of a few do not affect the consequent shock breakout due to the dominance of electron scattering at the shock breakout region.

OPAL provides an effective opacity, including absorption and scattering. However, CASTRO RHD calculation requires absorption ($\kappa_{\nu,ab}$) and scattering ($\kappa_{\nu,sc}$) opacities, independently. Therefore, the absorption opacity is obtained from the three dominant absorption opacity sources following Lovegrove et al. (2017) including bound-free ($\kappa_{\nu,bf}$), free-free ($\kappa_{\nu,ff}$) and consider Compton scattering from a tiny fraction of electron scattering ($\epsilon \times \kappa_{es}$, where $\epsilon = 10^{-4}$) assuming the fraction of photon energy can be transferred to the gas during photon-electron collisions. These opacities depend on the gas temperature (T , K) and density (ρ , g cm^{-3}) in the form:

$$\kappa_{\nu,bf} \propto \rho^2 T^{-0.5} \nu^{-3} Z(1 + X), \quad (2)$$

$$\kappa_{\nu,ff} \propto \rho^2 T^{-0.5} \nu^{-3} \frac{Z^2}{\mu_e \mu_I}, \quad (3)$$

$$\kappa_{es} = \rho_e K_{sc} \left[1 + \left(\frac{T}{4.5 \times 10^8 \text{ K}} \right)^{0.86} \right]^{-1} \times \left[1 + 2.7 \times 10^{11} \frac{\rho}{T^2} \right]^{-1}. \quad (4)$$

μ_e is the mean molecular weight of electrons, μ_I is the mean molecular weight of ions, and ρ_e is the electron density. We consider partial degeneracy at a high-temperature regime for Thomson electron scattering opacity $K_{sc} = 0.4 \times \rho \times Y_e$, where Y_e is the electron fraction (Buchler & Yueh 1976). Then, we obtain the scattering opacity with the effective opacity from OPAL $\kappa_{\nu,OPAL}$

$$\kappa_{\nu,sc} = \kappa_{\nu,OPAL} - \kappa_{\nu,ff} - \kappa_{\nu,bf} - \epsilon \kappa_{es}. \quad (5)$$

If the effective opacity is unavailable from the OPAL table for a certain temperature and density region, we assume $\kappa_{\nu,ab} = \kappa_{\nu,bf} + \kappa_{\nu,ff} + \epsilon \kappa_{es}$; $\kappa_{\nu,es} = (1 - \epsilon) \kappa_{es}$ to fill the opacity gaps of OPAL. This setup provides a realistic frequency-dependent opacity in our 2D simulations.

2.2. Progenitor Star Models of SN 1987A

2.2.1. Single-Star Progenitor Model

We adopt the single-star progenitor of SN 1987A from Lovegrove et al. (2017), which was computed using the stellar evolution code, KEPLER (Weaver et al. 1978). During the iron core collapse phase, a thermal bomb of 2.3×10^{51} erg is injected at the outer boundary of the iron core to initiate a successful explosion with a kinetic energy of $\sim 2 \times 10^{51}$ erg at the breakout. This process generates a strong shock driven by radiation, eventually leading to the complete destruction of the star. Subsequently, we map the 1D KEPLER explosion profile onto the 2D CASTRO $r - z$ coordinate system at the moment when the shock reaches 1×10^{12} cm, with a shell size of approximately $\sim 5 \times 10^{11}$ cm and a shock speed of $4 \times 10^8 \text{ cm s}^{-1}$.

2.2.2. Explosion with a nearby Companion Star

Recent studies (Menon et al. 2019; Ono et al. 2020; Orlando et al. 2020; Utrobin et al. 2021) have suggested that the progenitor star of SN 1987A may have formed in a binary system. This finding has motivated us to investigate the influence of a companion star on the explosion dynamics. Therefore, we assume a binary system in which the progenitor star of SN 1987A explodes, surrounded by a companion star.

To examine the shock breakout in this hypothetical binary system, we place a companion star near the SN 1987A progenitor star in a steady wind CSM from the primary (described later in §2.3), while ignoring the wind from the companion. The companion star is a $13 M_{\odot}$ main-sequence star with a radius of 5×10^{11} cm, located at a distance of 7×10^{12} cm from the SN 1987A progenitor star. This distance from the primary is consistent with typical separations in interacting binaries suggested by Tsai et al. (2023). The companion star has a surface temperature of $\sim 5 \times 10^4$ K, corresponding to $\sim 3 \times 10^5 L_{\odot}$, which is three times brighter than the observed SN 1987A progenitor (Podsiadlowski 2017). For this binary simulation, we use a 2D Cartesian coordinate system. The model with the binary companion is denoted as B.

2.3. Stellar Surface and Circumstellar Medium

The simulation box is extended to accommodate the shock interaction with the stellar surface and the CSM. For our single-star progenitor, it extends to 1×10^{14} cm on each side, while for the binary system, it is set to 4×10^{13} cm to resolve the binary structure. We fill the medium between the stellar surface and inner CSM from 3.2×10^{12} cm to 2×10^{13} cm using an interpolation scheme in Lovegrove et al. (2017).

The regions beyond 2×10^{13} cm are filled with CSM based on a steady wind profile of

$$\rho(r) = \frac{\dot{M}}{4\pi r^2 v_w}, \quad (6)$$

where the mass loss rate $\dot{M} \approx 8 \times 10^{-6} M_{\odot} \text{ yr}^{-1}$, stellar wind velocity $v_w \approx 450 \text{ km s}^{-1}$, and the radius r . These values follow the observational constraint and the BSG wind profiles (Chevalier & Fransson 1987; Sugerman et al. 2005). Moreover, we create various stellar wind profiles by adjusting the mass loss rate via $\alpha \dot{M}$, where $\alpha = [0.1, 0.2, 0.5, 1.0, 2.0, 5.0, 10]$. These profiles serve as the foundation for our investigations into the influence of the CSM on observable aspects of shock breakouts. The model with only the steady wind in the CSM are denoted as T. For the models in this study, α is set to 1.0 as the fiducial value except for the comparison in §4.3.

The observed asymmetries in the nebula of SN 1987A (e.g., Sugerman et al. 2005) inspire us to investigate the gas dynamics of SN explosions in inhomogeneous CSM environments. Such environments may naturally arise from stellar evolution and the formation of CSM. In addition to considering the binary companion, we also independently account for perturbations and an eruptive mass loss in the implemented BSG progenitor star and the steady wind CSM system.

2.3.1. Sources of gas inhomogeneity

The envelopes of massive stars can be highly convective and may not be aware of the collapsing core before the shock arrives (Chen et al. 2013; Mao et al. 2015). To assess the effects of inhomogeneities that may be introduced in such environments, we initialize density perturbations in the envelopes to evaluate their consequences on shock breakout. We introduce 2D density perturbations from the base of helium layer where the shock emerges to the stellar radius ranging over $6.2 \times 10^{10} \text{ cm} \leq r \leq 3.2 \times 10^{12} \text{ cm}$ to mimic the inhomogeneities: $\rho(r, \theta) = \rho_0(r)[1 + s \cos(m\theta)]$. To conserve momentum, we encompass sinusoidal perturbations $s \cos(m\theta)$ to create different perturbation modes, with $m = 32$ and $s = 1\%, 3\%, 5\%, 10\%, 15\%, 20\%, 25\%$, and 30% , s represents the amplitude of perturbed density $\approx \delta\rho / \langle \rho \rangle$. Since seeding initial perturbations aim to trigger mixing, perturbations are only added to the steady wind CSM, which has a homogeneous density. The models with the perturbation strength $s = 5\%$ are denoted as P.

2.3.2. Circumstellar Medium Structure from Eruptive mass loss

The late-time evolution of massive stars may involve eruptive mass loss through gravity waves or unstable nuclear burning (Woosley et al. 2007; Chen et al. 2014; Leung et al. 2021). Previous observations of interacting supernovae have suggested that a dense shell forms before the star dies. This shell likely resembles a disk or ring surrounding the progenitor star (Levesque et al. 2012; Yamaguchi et al. 2021). To simulate the effect of this ring-like dense shell during the shock breakout, we introduce a ring-like structure around the SN 1987A explosion model. The ring is placed in the steady wind CSM ($\alpha = 1.0$) at a distance of 5.0×10^{13} cm from the 1987A progenitor star, with an elliptical

Table 2. Summary of model setup and naming

Model	Description	Wind	α
(1)	(2)	(3)	(4)
N	1D normal spherical simulation.	steady wind	1.0
T	2D test simulation.	steady wind	1.0
P	2D simulation with perturbation strength 5%.	steady wind	1.0
R	2D simulation with a ring-like CSM.	eruptive mass loss wind	1.0
B	2D simulation with a companion star.	steady wind	1.0

NOTE—The summary of model names and their setups. N stands for “(N)ormal”, T stands for “(T)est”, P stands for “(P)erturbation”, R stands for “(R)ing-like” CSM, and B stands for “(B)inary”. For above-mentioned models, the strength of steady-wind of $\alpha = 1$ is applied unless specified with *. The detailed setting of each model can be found in §2.

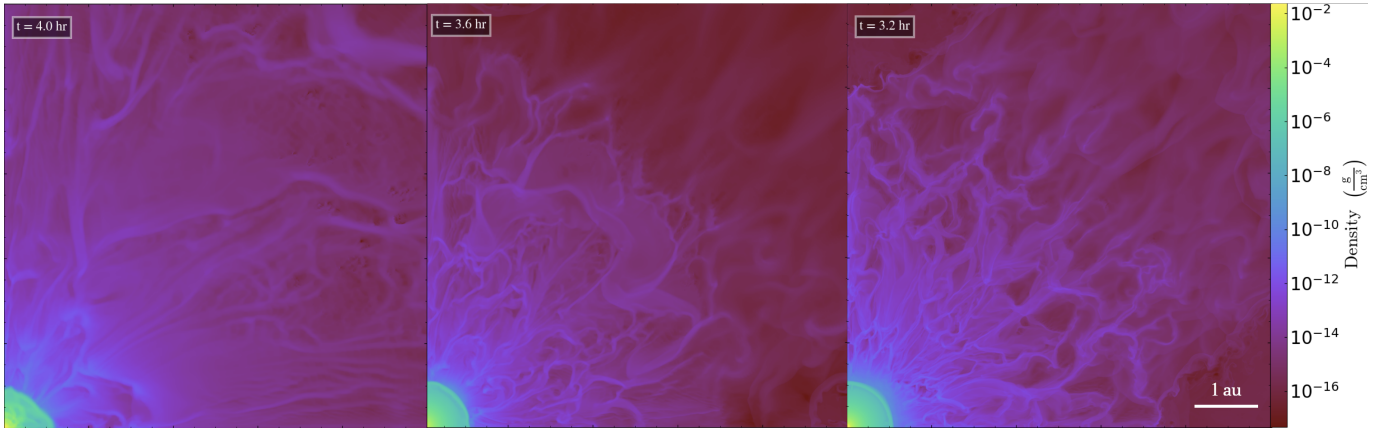


Figure 1. Resolution comparison of Model R. **Left:** Resolution of 512^2 . After the shock breakout, the inner supernova ejecta (the remnant) deviates from the spherical symmetry. **Middle:** Resolution of 1024^2 . The filaments and layers of the shock front are reasonably resolved. The difference between 512^2 and 1024^2 is more detailed filamentary structures that grow from small perturbations into large-scale mixing. **Right:** Resolution of 2048^2 . Although 2048^2 resolves more fine filamentary structures, it looks similar to 1024^2 . These tests suggest the optimal resolution is close to 1024^2 .

cross-section of major axis 10^{13} cm and minor axis 10^{12} cm. The density of the ring is set to be 100 times denser than the surrounding CSM based on the wind profiles. The model is denoted as R. Hereafter, we present several models of 2D simulations, the naming and the descriptions of models are summarized in Table 2.

3. VERIFICATION OF RADIATION HYDRODYNAMICS WITH RESOLUTIONS AND PERTURBATIONS

3.1. Resolution

To assess the influence of resolution on the results, we compare the density structures from simulations at grid resolutions of 512^2 , 1024^2 , and 2048^2 for a specific case, as depicted in Figure 1. We examine the density structures in two representative regions to assess the resolution at different distances from the star. One region encompasses the remnant, which should expand spherically throughout the shock breakout process. The other region is outside the remnant, where a shocked shell and filamentary gas structures should form in the post-shock region. Their density structures converge around the resolution of 1024^2 . Among all the resolution tests in Figure 1, their shock breakout duration and peak luminosity are similar, indicating that the physics of shock breakout is well resolved in our simulations with a resolution of 512^2 or higher. However, the angular-dependent LCs in Figure 2 show a significant difference between 512^2 and the other two resolutions, indicating that lower resolution may lead to unresolved structures

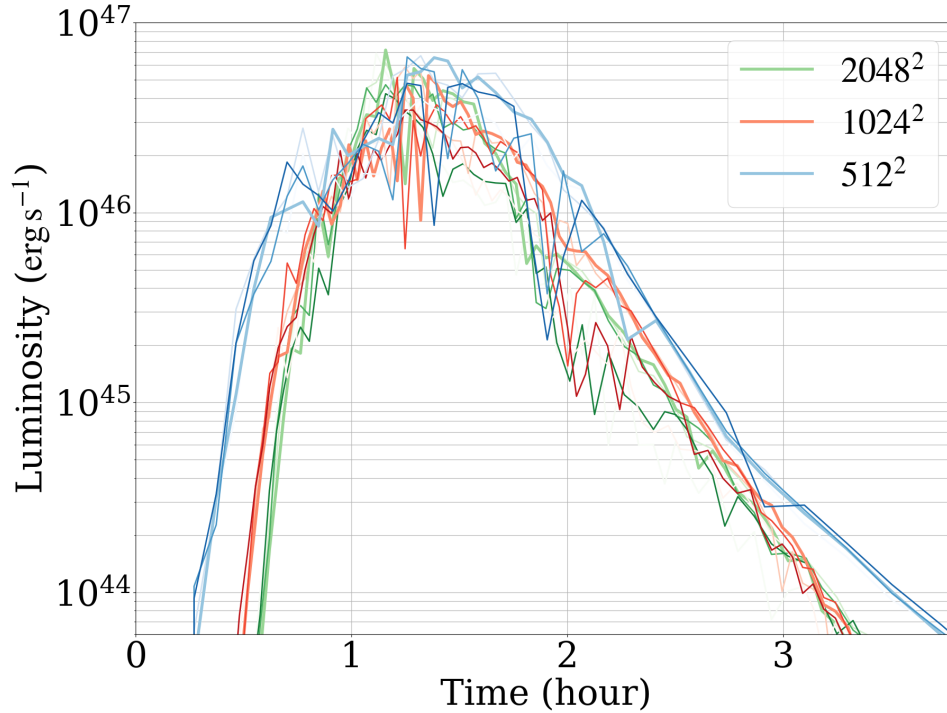


Figure 2. LCs from the Model R with different resolutions. The figure presents the band-VIII LCs at different viewing angles with selected colors, greens for 2048^2 , reds for 1024^2 , and blues for 512^2 . The bold line of each color represents the LC from the 45° viewing angle. Although the shock duration and peak luminosity from current resolutions are similar, the results from 512^2 deviate more from 2048^2 and 1024^2 , indicating insufficient resolution can affect shock breakout emissions.

that impact the breakout emission. We use a resolution of 1024^2 for our simulations presented in later sections to optimize the scientific outputs and the cost of computing resources.

3.2. Effect of Initial Perturbations

To assess the overall impact of the perturbations, we examine the influence on the shock breakout durations and peak luminosities for different perturbation amplitudes in Figure 3. We examine the sinusoidal perturbations with the amplitudes of $s = 1\%$, 3% , 5% , 10% , 15% , 20% , 25% , and 30% in the gas density. Figure 3 shows the shock breakout durations and peak luminosities stay almost unaffected by small perturbation amplitudes ($s = 1 - 5\%$). Meanwhile, for large perturbation amplitudes $\geq 10\%$, the peak luminosities and shock breakout durations can oscillate. Generally speaking, higher shock breakout duration is associated with lower peak luminosity, as higher luminosity implies stronger radiation flux leakage, resulting in a shorter breakout time. For $s \geq 10\%$ as seen in Figure 3 and Figure 4 (snapshots of the density for $s \geq 10\%$), such a strong perturbation may stimulate more nonlinear structures, increasing peak luminosity and shortening shock breakout duration, the choice of perturbation amplitudes may affect the structure formation for large perturbations. Therefore, our study focuses on small perturbations of $s \leq 5\%$ to ensure our simulations' shock breakout duration, peak luminosity, and structures are insensitive to perturbation strengths. Specifically, we choose $s = 5\%$ in this study.

3.3. RHD and Radiation Precursor

RHD is essential for modeling SN shock breakout, where radiation transport significantly affects gas dynamics as the gas becomes optically thin, $\tau \approx 1$. Figure 5 displays density and radiation-to-gas pressure ratio profiles, along with optical depths, from Model T. It is evident that the region around the forward shock is becoming optically thin, with its radiation-to-gas pressure ratio exceeding 10^3 .

Before the shock breakout peaks in LCs, the shock communicates with pre-shocked regions through radiation precursor (Epstein 1981), and the radiation temperature in the pre-shocked regions increases as shown in Figure 6. Due to the radiation precursor interaction with the pre-shocked region, the breakout shock has a smoother temperature gradient. Furthermore, in 2D, radiation pressure behind the shock varies from viewing angles, which affects fluctua-

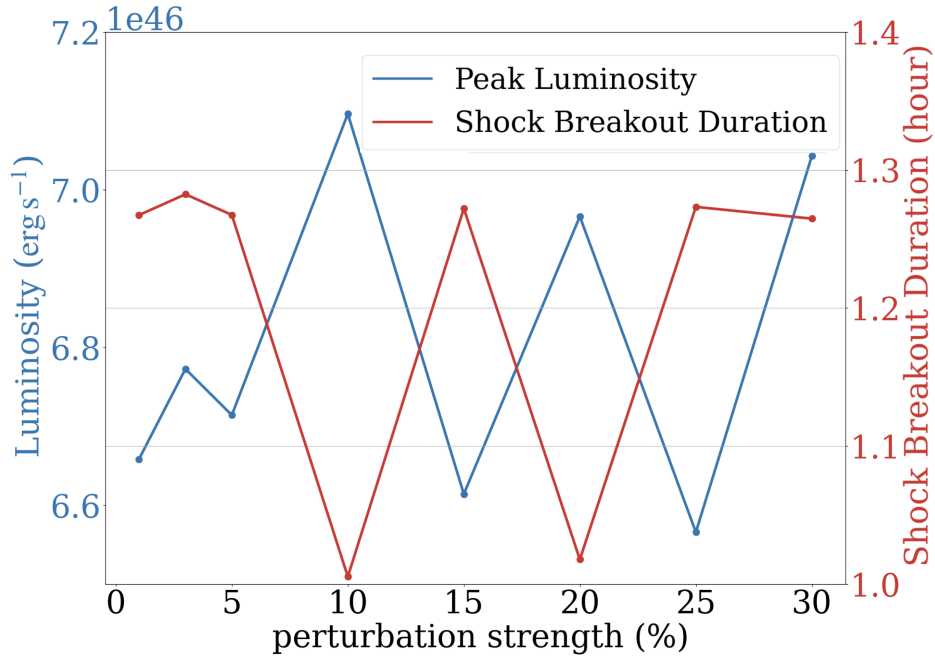


Figure 3. Band VIII peak Luminosity and shock breakout duration plot over different perturbation strengths (P; $s = 1\%$, 3% , 5% , 10% , 15% , 20% , 25% , and 30%). For small perturbations of $s \leq 5\%$, the outcomes are stable, while for stronger perturbations of $s \geq 10\%$, the peak luminosities and shock breakout durations have periodic fluctuation. In general, the stronger the peak luminosity, the shorter the shock breakout duration. We limit the strengths to be small to explore the general impacts of the perturbation.

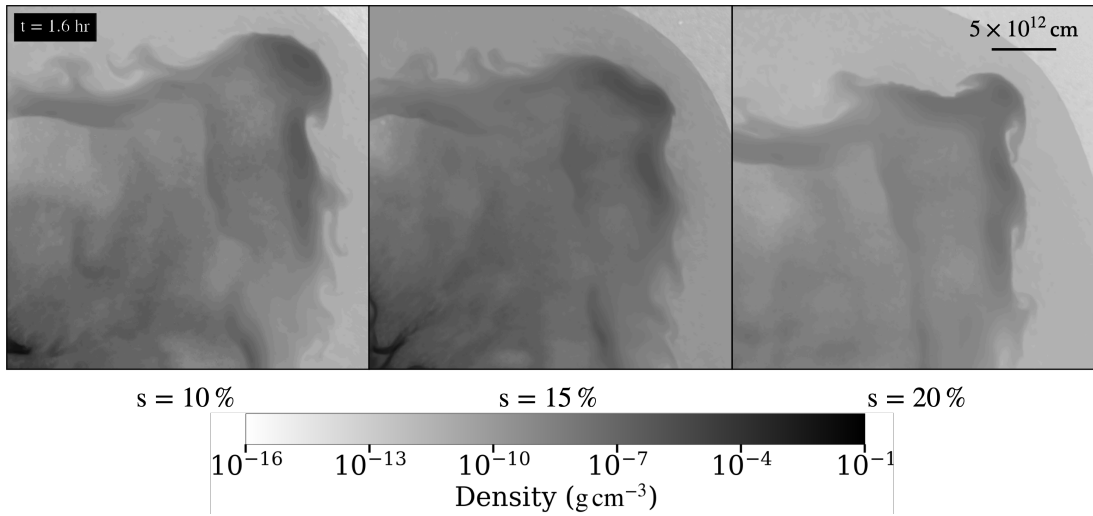


Figure 4. Zoom-in density plot for three perturbation strengths of $s = 10\%$, 15% , 20% , at around 1.6 hours. The left and right panels clearly show Rayleigh-Taylor instabilities in the reverse shock. Overall, three different strengths of perturbations lead to a consistent density distribution.

tions in density structures and shock breakout signals. Therefore, RHD simulations are required to model the shock breakout.

4. SHOCK BREAKOUT WITH STEADY WIND CSM

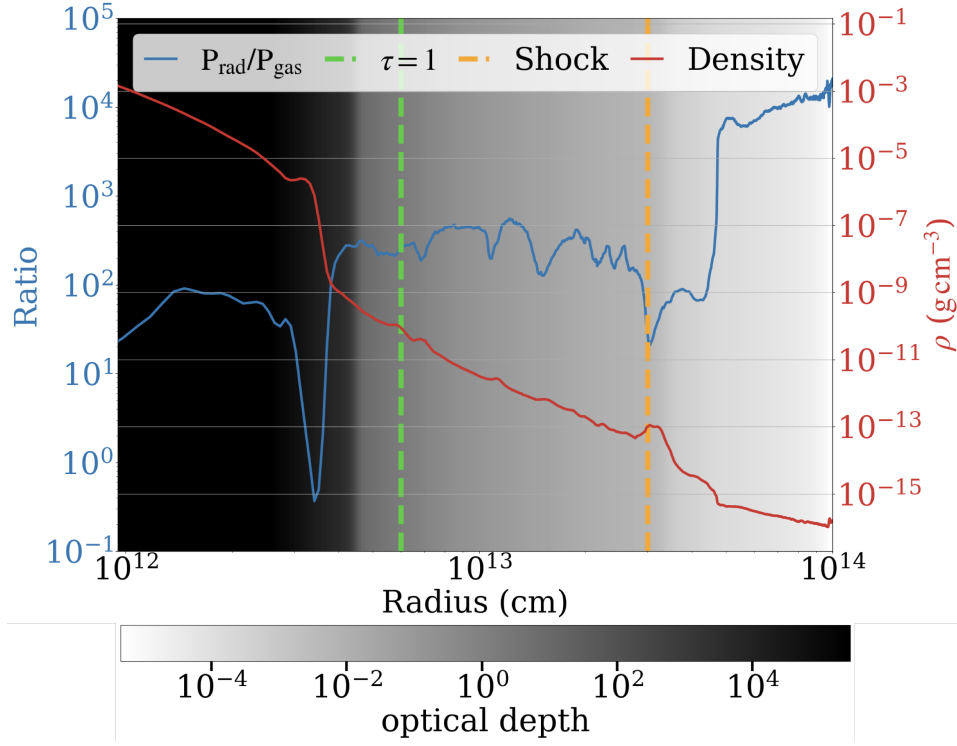


Figure 5. The 1D radial profile of Model T when the shock travels to 3×10^{13} cm (orange-dotted line). The background gray-scale color map shows the transition of optical depth (τ) from thick to thin, and the green-dotted line shows the position where $\tau = 1$. We show the radiation pressure to gas pressure ratio and gas density. The radiation pressure largely exceeds the gas pressure throughout the simulation regions.

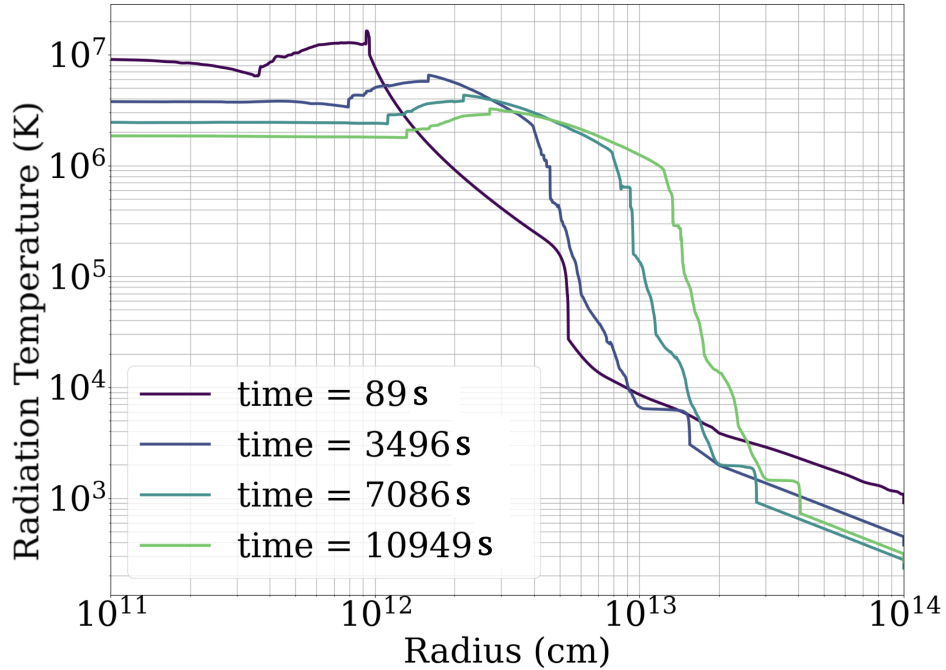


Figure 6. 1D radiation temperature profiles of Model T. The temperature is derived from the radiation energy from snapshots of our simulations. It demonstrates the influence of the radiation precursor on the pre-shocked region. As the shock propagates from the initial position at approximately 8×10^{11} cm to the later stage around 2×10^{13} cm, there is a noticeable reduction in the temperature gradient around the shock front due to radiation precursor heating.

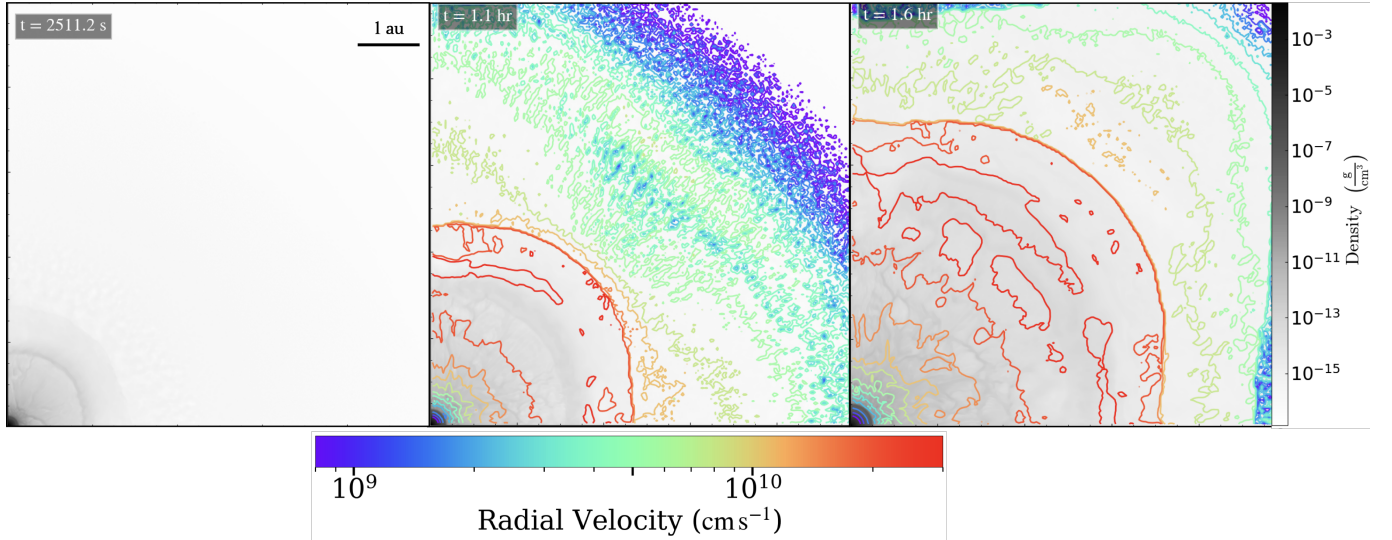


Figure 7. Three density snapshots of Model T with radial velocity contour, the left panel is plotted without contour to clearly depict the density structure. The structure is rather spherical and symmetric with a few turbulent structures.

Here, we briefly describe the results of the breakout simulation with steady wind CSM and zero perturbation (T) in Figure 7. The explosion shock propagates nearly spherically in the 2D space, while the reverse shock induces turbulence behind the forward shock colliding with the steady wind CSM. We use Model T as a reference for comparing shock structures, shock breakout duration, and peak luminosity across different 2D models (P, R, and B). The selected LCs for comparison are from the band, VIII of a wavelength of $\lambda = 7.12 \times 10^{-1} \text{ \AA}$ which dominates the peak luminosity of shock breakout (see Table 1), unless specified. The shock breakout duration and the peak luminosity are 1.54 ± 0.07 hour and $(2.7 \pm 0.4) \times 10^{46} \text{ erg s}^{-1}$, respectively. The breakout duration starts when the luminosity reaches 10% of the peak luminosity, and ends when it drops to 10% of the peak luminosity after passing the peak. The shock breakout duration is longer by a factor of ~ 5 compared to our 1D simulation (N) and previous 1D calculations (Ensman & Burrows 1992; Matzner & McKee 1999; Lovegrove et al. 2017). The details of 2D effects will be discussed in § 7.

The thin, dense shell found in the 1D calculation is broadened due to the development of fluid instabilities in 2D, which relax the dense shell to form fluid instabilities and post-shock mixing. However, the reflective boundaries can generate numerical artifacts that cause nonphysical mixing. Therefore, to minimize nonphysical mixing, we select the LCs of $\theta = 45^\circ$ as representative for comparison. Hereafter, we present the simulation results with perturbations strength 5% (P) as a representative case by showing the gas dynamics and LCs in the following subsections.

4.1. Gas Dynamics

As shown in Figure 8, introducing perturbations allows us to explore how the initial inhomogeneities in the gas originating from the star affect the shock breakout propagation in the CSM. For the panel around 2400 s, when the shock travels roughly spherically to $r \sim 3 \times 10^{13} \text{ cm}$, the reverse shock creates a large mixing area behind the shock. The initial sinusoidal perturbations evolve within both the shock front and the reverse shock regions. The thickness of the radiating shell is modified by bumps that can increase the radiation flux leakage and shorten the duration of breakout emission at different viewing angles. The middle panel shows a density bulb moving at high velocity because the shock first breaks out of the stellar surface around $\theta \sim 45^\circ$. Then, the gas behind the shock front suddenly accelerates to high velocity $v_r \sim 2 \times 10^{10} \text{ cm s}^{-1}$ and forms a blob of high-speed gas. After the shock breakout, the initial fluctuation seeded in the ejecta starts to grow quickly due to the Rayleigh-Taylor instabilities driven by the formation of a reverse shock.

To quantitatively describe the fluid dynamics, we plot the 1D velocity and density profiles of different viewing angles in the middle panel of Figure 8 in Figure 9 (as in Sharma et al. 1987). The steep radial velocity jump is the shock front. The shock velocity is at $\sim 10^{10} \text{ cm s}^{-1}$, slightly varying among different viewing angles due to perturbation. It implies that the shock breakout occurs at different times and causes differences in LCs among viewing angles. Also, the perturbations evolve into the density bump shown in the 45° curve, and the radial velocity is also higher at this

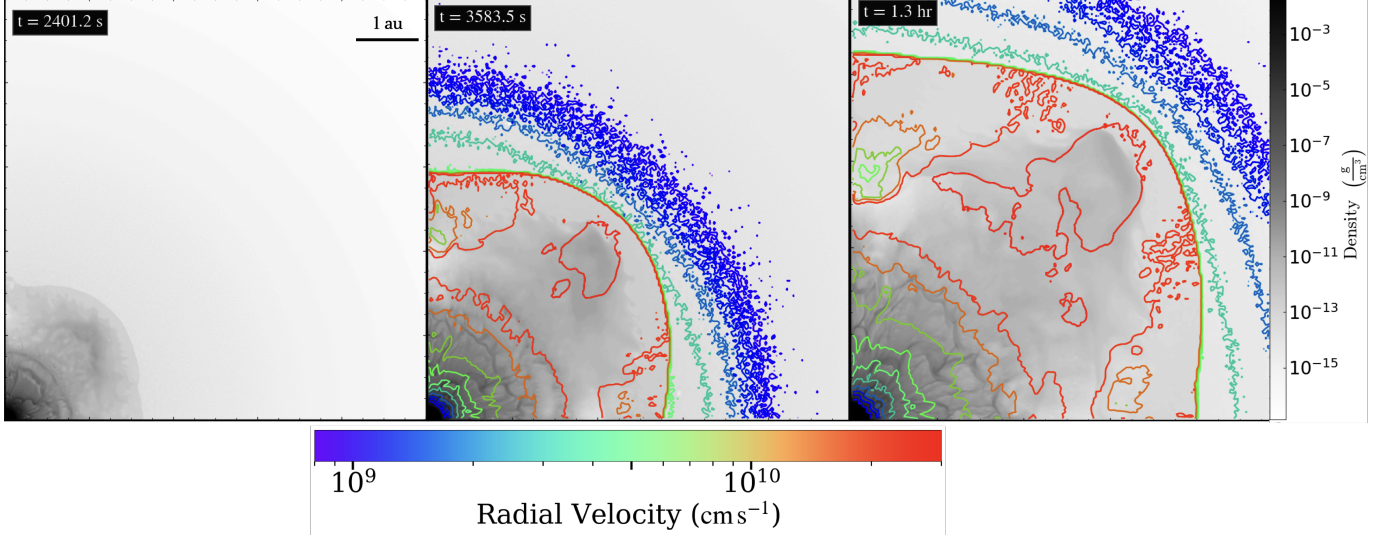


Figure 8. Same as Figure 7 but for Model P. Three panels at different times show the evolution of perturbation seed into larger structures.

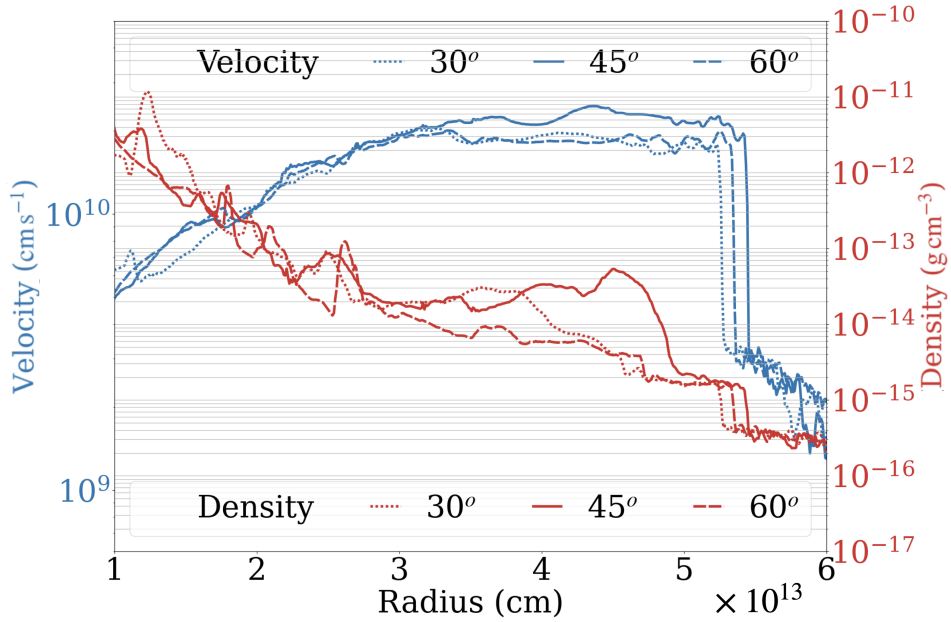


Figure 9. 1D velocity and density profiles at three different angles for Model P. The shock front is depicted as the velocity jumps at 5×10^{13} cm. Due to the strong mixing in the post-shock region, the density profiles vary significantly across different viewing angles.

region. In the filament regions around $(1 - 3) \times 10^{13}$ cm, there are density fronts that also present on the velocity contour of the middle panel in Figure 8; their positional deviations result from encountering evolved perturbations.

In Figure 9, the sparse low-velocity regions ahead of the shock front are driven by radiation precursor. It may further enhance the mixing when the shock front passes. These phenomena are also seen between $(3 - 4) \times 10^{13}$ cm between filament regions and the reverse shock when the radiation precursor from the filament frontiers drives these regions. Because the radiation precursor originates from turbulent regions, the pre-shocked regions inherit these fluctuations and grow larger during shock propagation. The initial amplitude of the perturbation in the density is about 5%, which grows to a factor of few. Compare the initial profile with the right panel of Figure 8, the post-breakout density profile at 8×10^{13} cm increase from $1.3 \times 10^{-16} \text{ g cm}^{-3}$ to $4 \times 10^{-14} \text{ g cm}^{-3}$. During the shock breakout, only a tiny fraction of

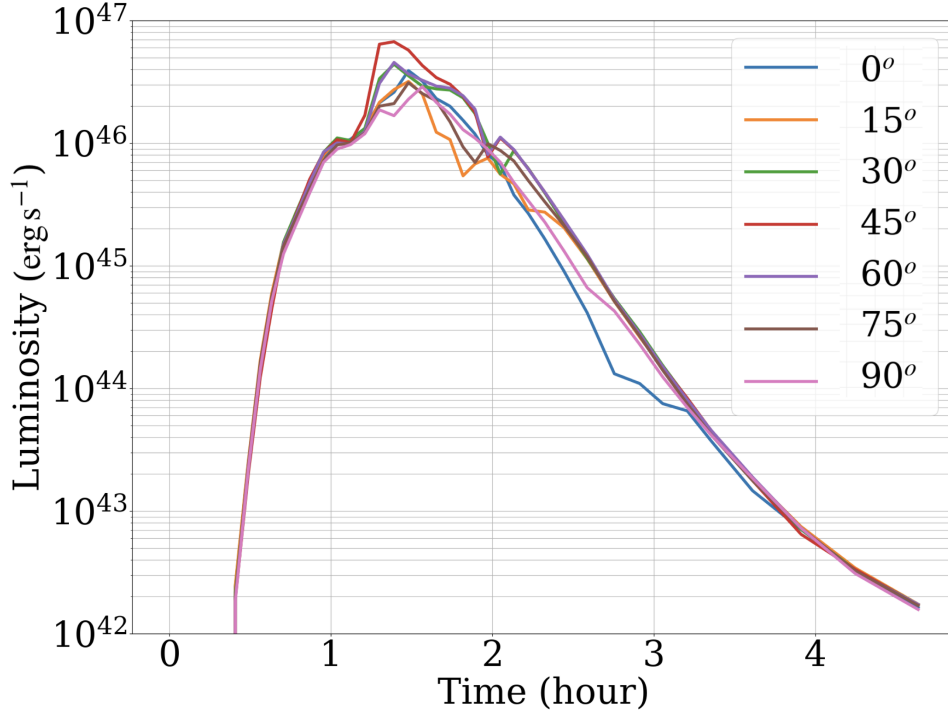


Figure 10. LCs of band VIII in viewing angles from Model P. The LCs show small deviations at the rising phase, then start to vary more after the peak due to the mixing

the mass, $2 \times 10^{-4} M_{\odot}$, is ejected, and most of the mass remains inside the slower moving remnant of the progenitor star.

4.2. Light Curves

In Figure 10 and Figure 12, we present the multi-color LCs with different viewing angles of Model P. The shock breakout duration is $\approx 0.93 \pm 0.12$ hours with a peak luminosity $(4.1 \pm 1.3) \times 10^{46} \text{ erg s}^{-1}$ among viewing angles. The angular-dependent LC (Figure 10) is essential in capturing the characteristics of multidimensional simulations and can reveal structure evolution. During the rising phase, the shock front is initially spherical symmetry. However, as the system evolves, the fluctuations grow due to the radiative cooling via radiation precursor, resulting in angle-dependent LCs. The co-evolution of radiation and gas impacts the breakout dynamics. The photosphere recedes when the shock expands and allows emission from the mixing regions. It enhances the fluctuations in LCs during the post-peak period. The non-uniform distribution of radiation flux vectors is shown in Figure 11.

Figure 12 shows LCs of different colors that show the evolution of the photospheric temperatures of the shock breakout. Based on the colors, their LCs peak with luminosities as follows (from I to VIII): 1.2×10^{40} , 3.4×10^{41} , 4.2×10^{42} , 2.9×10^{43} , 1.7×10^{44} , 2.2×10^{45} , 8.8×10^{45} , and $7.7 \times 10^{46} \text{ erg s}^{-1}$, respectively. Notably, peak luminosity increases by an order of magnitude with each successive wavelength band. The breakout duration for band I-VIII is 1.3, 1.2, 1.4, 1.3, 1.2, 0.5, 0.9, and 1.2 hours, respectively. Before the breakout, the luminosity variation among viewing angles is approximately 14%. The LCs of colors have a similar shape during the rising phase. However, LCs of longer wavelengths are more sensitive to viewing angles.

Post-breakout cooling becomes prominent after the LCs reach their peaks and the luminosity drops. For band VIII, the decline rate is $\dot{L} = 4 \text{ mag hour}^{-1}$. The dominant energy band shifts towards longer wavelengths, and the correspondent band V decline rate is $\dot{L} = 1.5 \text{ mag hour}^{-1}$, reflecting the expansion of the photosphere with a decreasing radiation temperature.

4.3. Effect of Steady Wind Strength

To examine the observational signatures of the shock breakout associated with the CSM formed prior to the explosion, we modify the density profiles by varying the mass loss rate as $\alpha \dot{M}$, where α takes values in the range

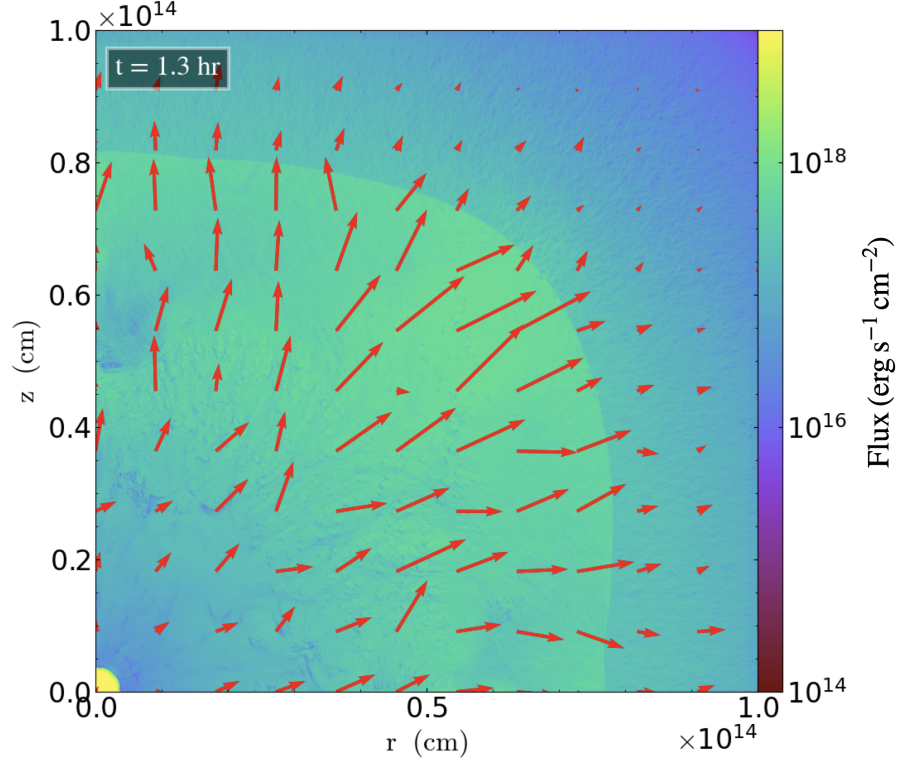


Figure 11. The radiation energy flux density and vector (red arrows) of band VIII for Model P. The magnitude of flux is maximum at the emitting region. Due to the strong mixing, the radiation vectors are misaligned with radial directions, and their magnitudes also vary with viewing angles.

of $[0.1, 0.2, 0.5, 1.0, 2.0, 5.0, 10]$, spanning two orders of magnitude as outlined in § 2. The correlation is depicted in Figure 13.

Despite the fluctuation, we observe that a higher α with a denser and extensive CSM prolongs the shock breakout duration and decreases its peak luminosity. We also derived a fitting formula of the peak luminosity with α that follows $L = -3.51 \log \alpha + 7.73$ ($10^{46} \text{ erg s}^{-1}$) and $\tau_{\text{shock}} = 0.443 \log \alpha + 1.25$ (hours), where τ_{shock} is the shock breakout duration. As α increases, the opacity increases in front of the shock, prolonging the shock breakout duration and dimming the peak luminosity.

Our 2D results can produce a shock breakout duration similar to a 1D breakout in the dense CSM environment found in Förster et al. (2018). Therefore, we suspect the shock breakout duration in the previous 1D shock breakout calculations is underestimated due to a lack of mixing effect.

5. SHOCK BREAKOUT WITH A RING-LIKE CSM

5.1. Gas Dynamics

We present the evolution of the shock breakout with the ring-like CSM (R) in Figure 14. In the left panel of Figure 14, the shock front travels to $4 \times 10^{13} \text{ cm}$, with radial velocity $\sim 2 \times 10^{10} \text{ cm s}^{-1}$. The thickness between the shock front and the reverse shock is $5 \times 10^{12} \text{ cm}$. At this moment, the ring does not influence the shock propagation. In the middle panel, the collision of SN shock creates a converging shock wave that wraps around the ring-like CSM. During the collision, a strong reverse shock forms and propagates back to the ejecta and drives a vigorous mixing, as shown by the filamentary structures in the left-bottom corner of the middle panel in Figure 14. When the shock approaches the boundary of the simulation box, the ring-like CSM is destroyed, and its debris starts to follow the forward shock at a velocity of $2 \times 10^{10} \text{ cm s}^{-1}$.

To better evaluate the gas dynamics, we present the 1D density and velocity profiles of the right panel of Figure 14 in Figure 15. Due to the hindrance of the ring-like CSM at 45° , the forward shock along 45° travels to $8 \times 10^{13} \text{ cm}$,

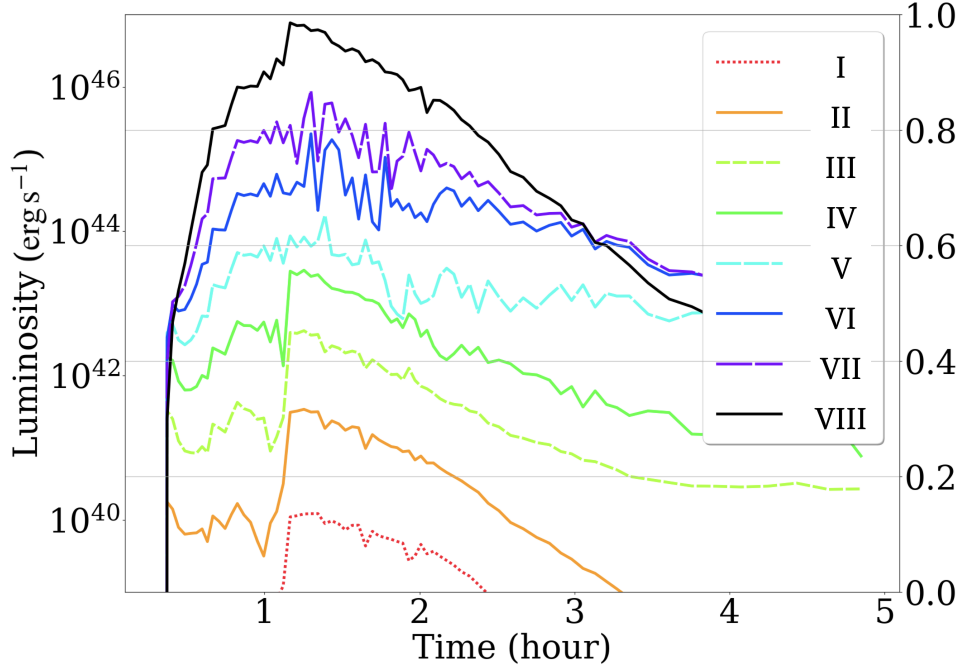


Figure 12. Color LCs of Model P at angle 45° . The number of bands represents frequency from band I 10^{13} Hz to band VIII 10^{18} Hz. The peak luminosity appears $6.71 \times 10^{46} \text{ erg s}^{-1}$ for the band VIII, and the corresponding duration is 1.27 hour. The dominant band VIII transits to lower frequency bands VII and VI at around 3 hours due to the shock cooling. The fluctuations start around the peak luminosity, followed by increasing bumps at lower wavelengths. These post-peak fluctuations are caused by mixing the post-shock regions in which the photosphere is located.

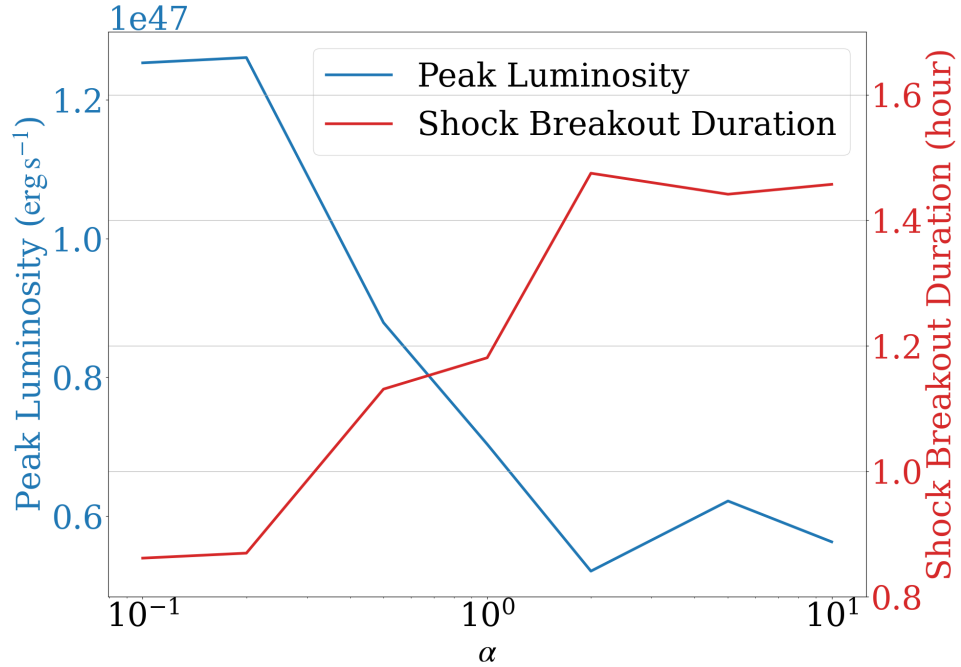


Figure 13. The the peak luminosity and shock breakout duration as a function of the mass loss rate parameter (P; $\alpha = 0.1, 0.2, 0.5, 1.0, 2.0, 5.0, 10$). Higher values of α correspond to denser CSM profiles. We find that shock breakout duration positively correlates with α : $\tau_{\text{shock}} = 0.443 \log \alpha + 1.25$ (hours). A dilute CSM tends to produce a higher peak luminosity with a shorter duration.

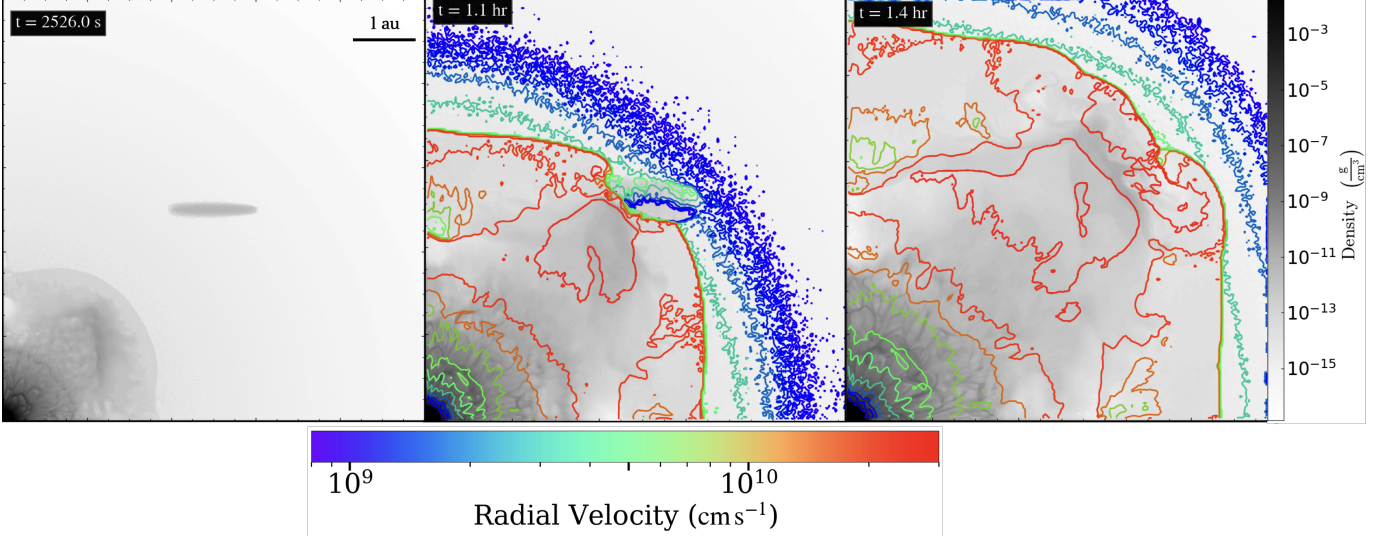


Figure 14. Same as Figure 7 but for Model R. The velocity contour shows strong turbulence and converging flows near the collision site. The middle panel reveals strong mixing around the reverse shock and shock front layer at $r = 8 \times 10^{13}$ cm. Finally, the ring-like CSM is fully destroyed by the shock, as shown in the right panel.

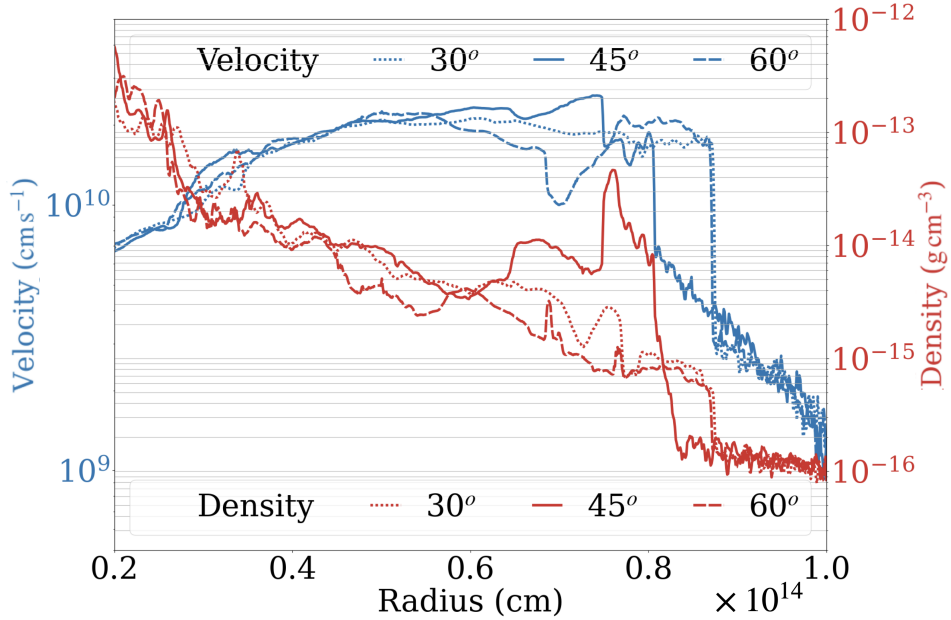


Figure 15. The velocity and density profile at three different angles in Model R. The velocity fronts at distances around 8.7×10^{13} cm and 8×10^{13} cm are the shock fronts. At 7.5×10^{13} cm of 45° , there is a reverse shock evolved from the collision of the ring-like CSM.

shorter than those in the directions of 30° and 60° . The impinging gas flow passing around the shocked ring creates shear instabilities and drives mixing.

5.2. Light Curves

We present multi-angle LCs in Figure 16 and the corresponding multi-wavelength LCs at 45° in Figure 17. Based on Figure 16, the shock breakout duration is $\approx 0.76 \pm 0.06$ hour with a peak luminosity of $\approx (4.8 \pm 0.8) \times 10^{46}$ erg s $^{-1}$ among viewing angles. In the rising phase of Figure 16, the radiation precursor interacts with the ring first and shows luminosity fluctuation before breakout. At the breakout phase, the ring blocks the highest energy band VIII between 30° and 60° around 1.3 hours, which leads to a significant deviation in LCs among different angles. The collision

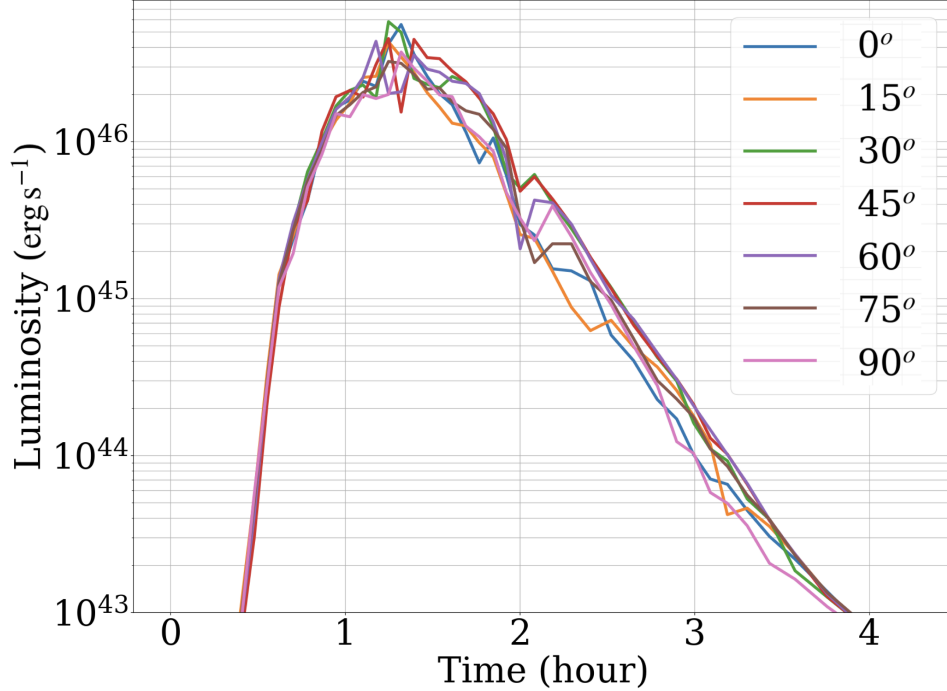


Figure 16. Same as Figure 10 but for Model R. The shock breakout duration is ~ 0.76 hours with peak luminosity at $\sim 6.0 \times 10^{46} \text{ erg s}^{-1}$. The LCs fluctuate at the rising phase due to radiation precursor interaction with the ring-like CSM. When the shock collides with the heated structures at around 1.5 hours, the ring blocks the radiation energy around 45° , creating a sudden drop near the luminosity peak.

of the shock front with the ring creates strong mixing and causes evident luminosity fluctuations at 2 hours among different viewing angles, as shown in Figure 16. These fluctuations can be seen for bands V and VI, around 1.8 hours, and band IV around 2.2 hours in Figure 17. The luminosity fluctuation is $\sim 18\%$ before the breakout point. After the shock collides with the ring, the luminosity fluctuation is $\sim 13\%$ for band VIII and $\sim 54\%$ for band VI, showing that the mixing regions significantly affect the emission of longer wavelengths. Although the ring structure may not survive after the shock collision, the multi-wavelength LCs of shock breakout may reveal some information about the pre-explosion environment.

In Figure 17, the peak luminosities of bands I to VIII are 6.8×10^{39} , 2.4×10^{41} , 3.0×10^{42} , 2.2×10^{43} , 9.1×10^{43} , 2.0×10^{45} , 9.3×10^{45} , and $5.3 \times 10^{46} \text{ erg s}^{-1}$, respectively. Their shock breakout durations are 1.3, 1.2, 1.6, 1.4, 1.1, 0.83, 0.83, and 1.4 hours, respectively. Despite different peaks and durations, the characteristic LC shape is similar for all bands. Due to the cooling of the shock, the dominant photon energy also switches from high to low at 3.0 hours. After the luminosity reaches the peak, it starts to decay at a rate of $\dot{L} = 3.5 \text{ mag hour}^{-1}$ for band VIII. For band V, the rate is $\dot{L} = 1.5 \text{ mag hour}^{-1}$. It only takes about 1.5 hours for the luminosity to drop from the peak to its 1% value.

6. SHOCK BREAKOUT WITH A COMPANION STAR

6.1. Gas Dynamics of Collisions

We show the density plots from the breakout simulation with the companion star (B) in Figure 18. The collision between the supernova shock and the companion star creates strong mixing in the contact discontinuity regions, and the surviving companion continues driving the post-breakout turbulence through its evaporating envelope.

In the left panel of Figure 18, the shock front passes through the companion star at $2.1 \times 10^{13} \text{ cm}$ with the radial velocity of $\sim 10^9 \text{ cm s}^{-1}$. Although the shock front is generally spherical, the companion star continues to drive the reverse shock instabilities. The post-shock mixing has grown to 10^{13} cm along the surroundings of the companion star and creates a valley of low-density region along the direction of 45° .

To analyze the interactions between the blast wave and the companion star, we present 1D profiles of different viewing angles at $\sim 1900 \text{ s}$ in Figure 19. The forward shock of the blast wave is at $2.1 \times 10^{13} \text{ cm}$, and the reverse

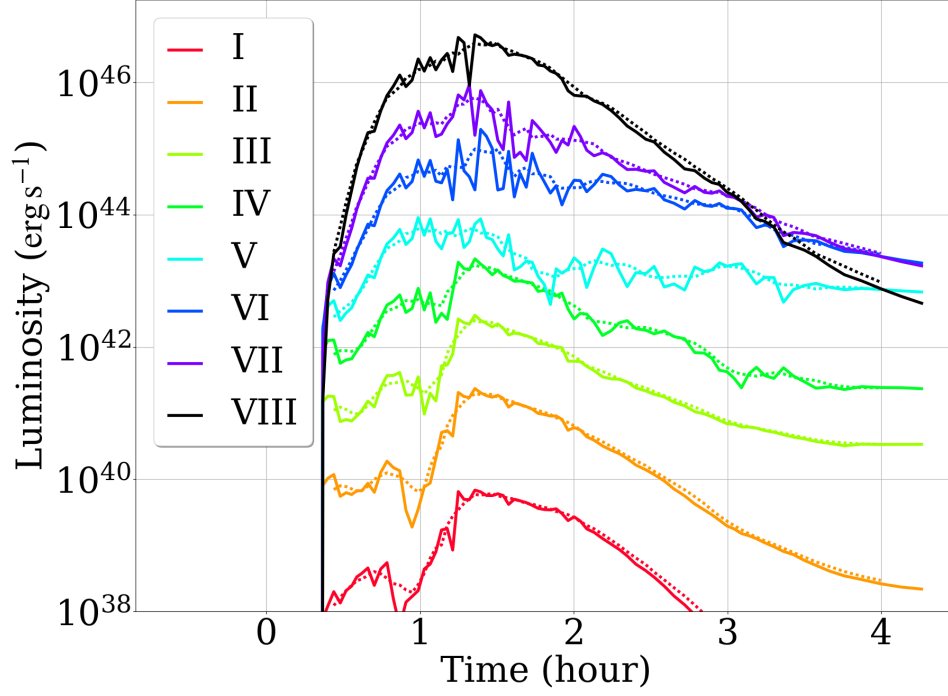


Figure 17. Same as Figure 12 but for Model R, the dotted curves are moving-averaged with ± 0.5 hours. Before the luminosity reaches a peak, the radiation precursor gradually heat up the ring-like CSM and create small bumps from band I at 0.7 hours to around 1.1 hours for bands IV, V, and VI. During the breakout phase, the ring-like CSM absorbs the band VIII radiation, redistributing radiation energy to lower frequency bands. The dominant band of emission transits to VII after ~ 3 hours of the shock breakout.

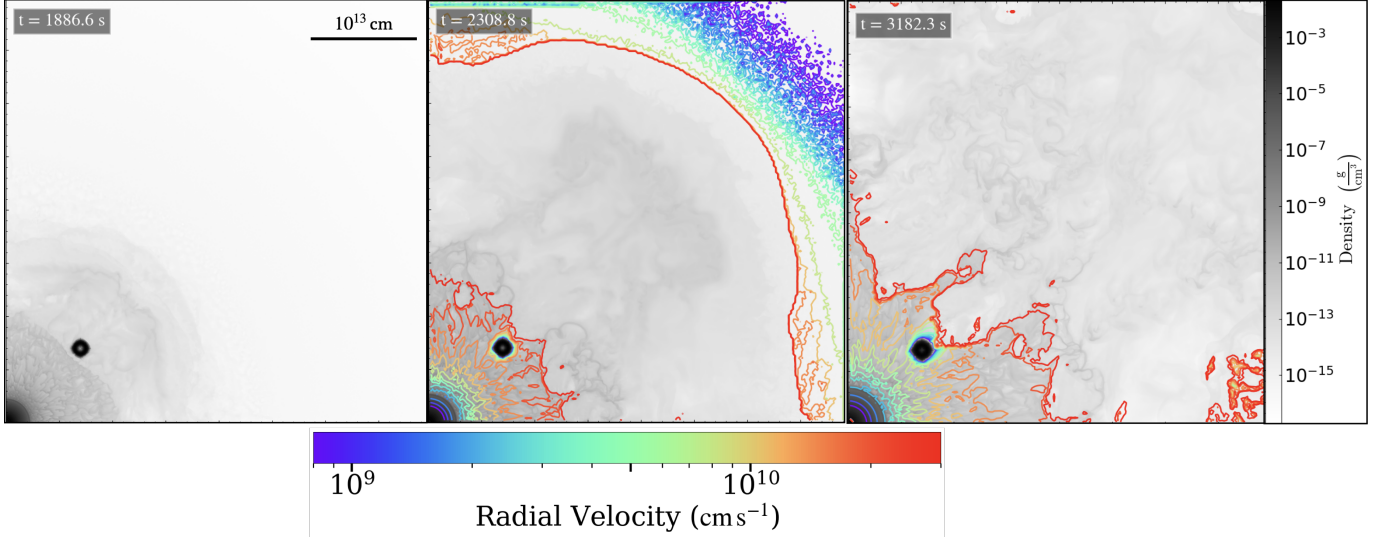


Figure 18. Same as Figure 7 but for Model B. The companion star can hinder the shock front and drive the turbulence through Kelvin-Helmholtz instabilities when the SN ejecta passes.

shock from the colliding companion is at $\sim (1.8-1.9) \times 10^{13}$ cm. Comparing different angle profiles, a more substantial reverse shock appears in 45° direction where the companion star is placed.

In the middle panel of Figure 18, the shock front passes the companion star and left a strong mixing region at ~ 2300 s. The robustness of the companion star blocks the shock flow and creates a low density region behind the companion star, creating fluid instabilities that turn into turbulence and fill the ambient space in the shadow regions.

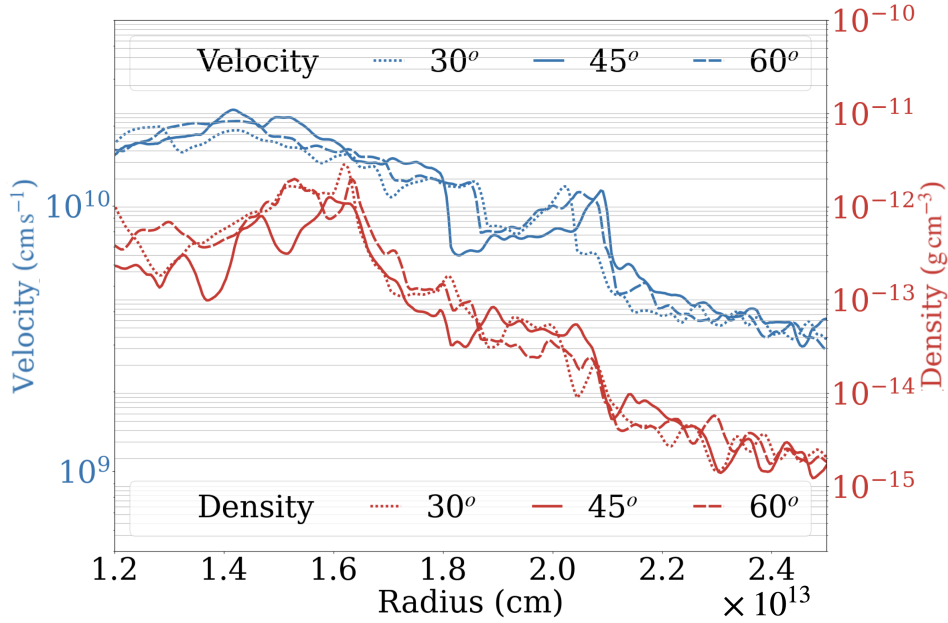


Figure 19. The velocity and density profiles of Model B at ~ 1890 s. At this time, the forward shock is at 2.1×10^{13} cm and the reverse shock is at 1.8×10^{13} cm. The collision of the companion star impacts the flow velocity along 45° direction.

In the right panel of Figure 18, the shear velocity between the companion star and SN ejecta creates Kelvin-Helmholtz instability. Further, it mixes the post-breakout gas behind the forward shock. The companion slightly expands due to the compressible heating by the shock.

We compare the density profiles before and after the shock collision with the companion in Figure 20, the radius of the companion star expands, and it loses around 25% of its initial mass. Previous studies show the effect of the impinging blast wave can strip and ablate mass from the companion star (Wheeler et al. 1975). Depending on $\Psi = \frac{1}{4} \frac{M_{\text{sn}}}{M_c} \frac{R^2}{a^2} \left(\frac{v_{\text{sn}}}{v_{\text{es}}} - 1 \right)$, where M_{sn} is the mass of supernova ejecta, M_c is the mass of colliding companion, R is the radius of the companion star, a is the initial separation, $v_{\text{sn}} \sim 2 \times 10^{10} \text{ cm s}^{-1}$ is the speed of SN ejecta and $v_{\text{es}} \approx \frac{2GM_c}{R}$ is the escape velocity on the surface of the companion star. Given that $M_{\text{sn}} \sim \frac{4\pi}{3} x^3 \rho$, where $\rho(x) \sim 10^{-6} \text{ g cm}^{-3}$ at $x \sim 6 \times 10^{12}$ cm from Figure 20, we calculate that $\Psi \approx 1$, which implies 15% to 30% strip and ablate mass loss for polytropic $n = 3$ star.

6.2. Light Curves

We show the resulting LCs in Figure 21 and Figure 22. The LC of the shortest wavelength has a peak luminosity of $(2.97 \pm 1.22) \times 10^{46} \text{ erg s}^{-1}$ with a shock breakout duration of 0.84 ± 0.09 hours. Due to the smaller box size of the binary simulations, we have to compensate the light travel time of ~ 1580 s to the binary LCs for comparison with the LCs of previous runs.

When the shock passes through the companion star, it remains spherical. Therefore, the rising phase of LCs shows slight angle fluctuation. After the shock passes through the companion star, the turbulence snowballs through the shear instabilities and the resulting mixing affect the propagation of radiation flux and create luminosity deviation. The post-shocked ejecta evolved into multiple layers, forming secondary luminosity peaks between $\approx 1.3 - 1.5$ hours, especially in the LC of 45° . For other angles, post-breakout mixing fluctuates the secondary peaks, and they appear at different times. The strong mixing and shadow effect from the companion star cause secondary peaks.

As seen in Figure 22, the peak luminosities for various bands (from I to VIII) are 1.4×10^{40} , 2.1×10^{41} , 1.8×10^{42} , 1.5×10^{43} , 1.1×10^{44} , 1.2×10^{45} , 6.0×10^{45} , and $4.3 \times 10^{46} \text{ erg s}^{-1}$, respectively. The corresponding shock breakout durations are 0.67, 0.85, 1.2, 0.76, 0.53, 0.65, 0.61, and 0.81 hours, respectively. The overall patterns show smaller fluctuations in higher wavelengths, and the luminosity can vary up to $\sim 44\%$ around the peak for band VI. On the other hand, the fluctuation is minimized to $\sim 14\%$ for band VIII.

The peak luminosity appears at ~ 1 hour for all wavelengths, while the second peaks occur at 1.24 hours for band I to band V and 1.21, 1.28, and 1.35 hours for band VI to VIII. The secondary peak arises from the envelope heating

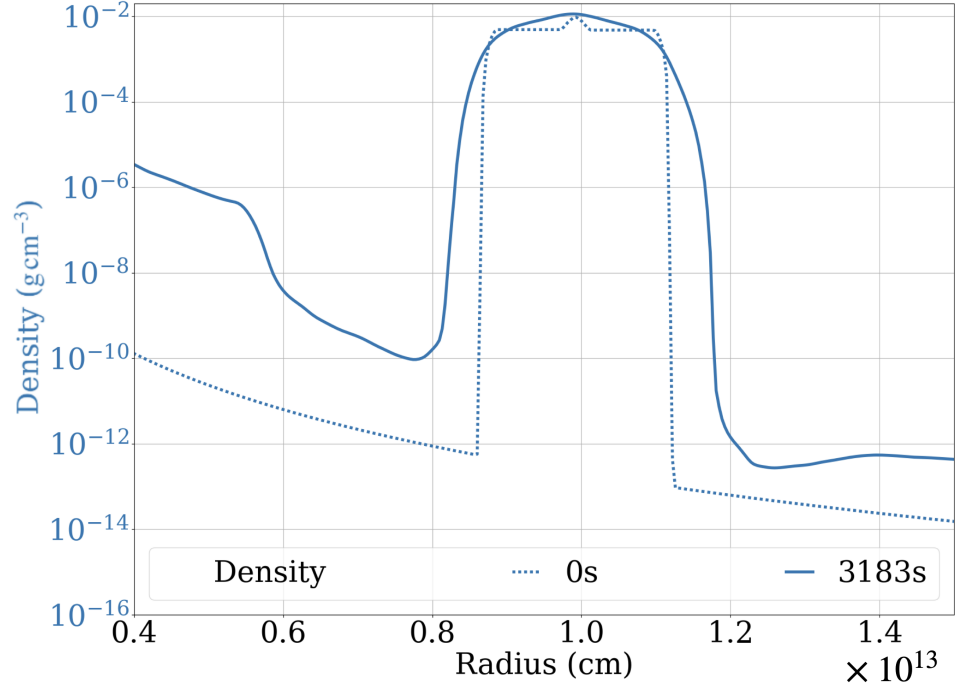


Figure 20. Density profiles of Model B before and after the shock collision, the left panel is plotted without contour to show the density structure. Due to the shock heating, the companion expands around 25% in size, and the heated envelope of the companion partly escapes through ablation and strip.

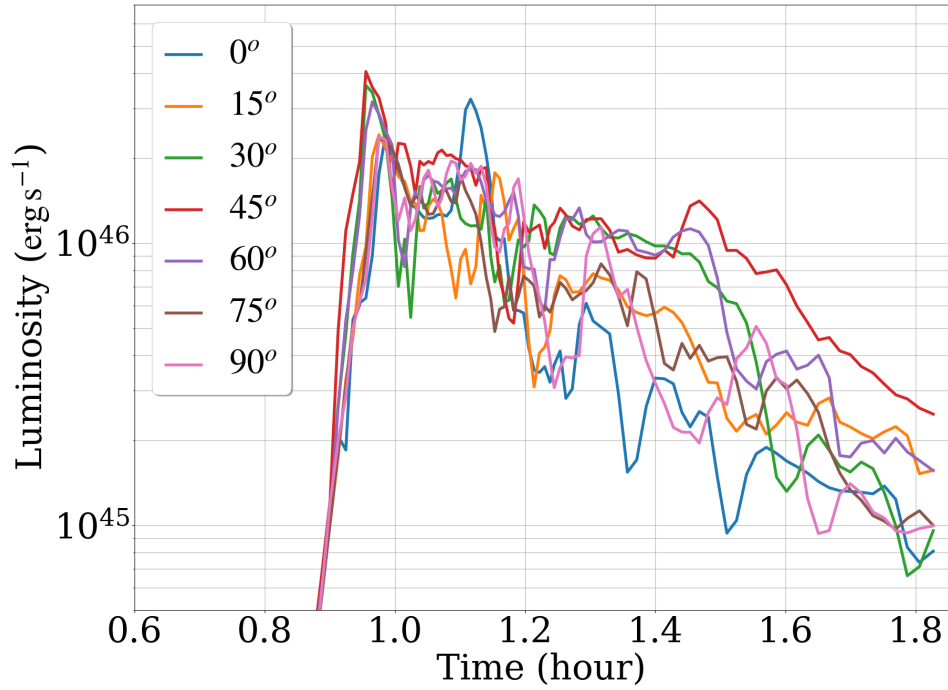


Figure 21. Same as Figure 10 but for Model B. Small fluctuations appear in the rising phase, then soon grow into large variations because of the strong mixing driven by the companion.

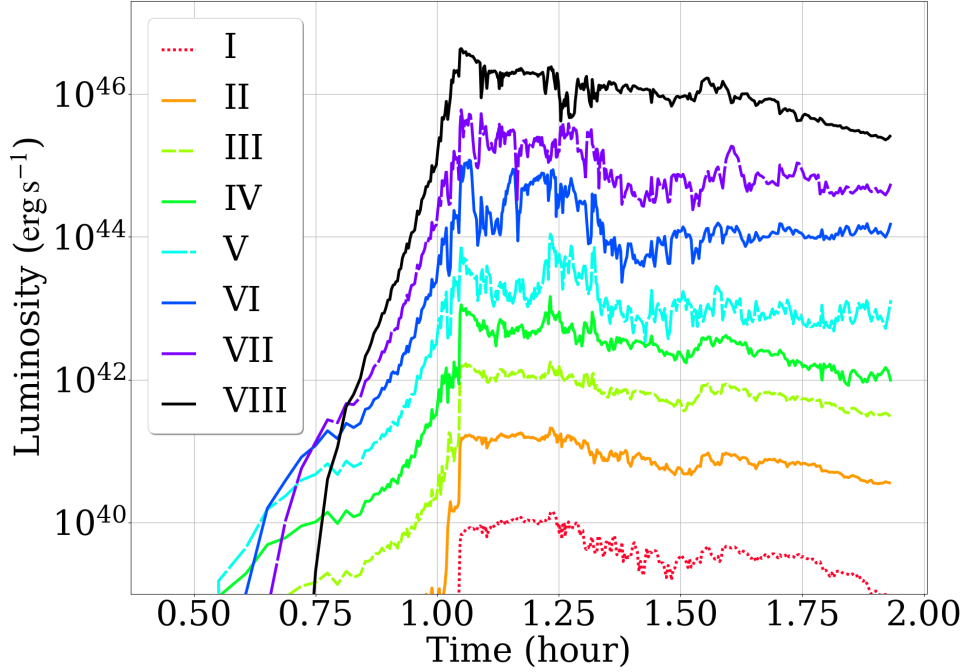


Figure 22. Same as Figure 12 but for Model B. Here, we compensate for the light traveling time of ~ 1580 s because the box is smaller for this simulation. The companion absorbs and blocks the high energy, then releases the emission of longer wavelengths at 1.25 hours. Double peaks are observed in each band, and the second peaks are more prominent for longer wavelengths.

Table 3. Shock Breakout Durations and Peak Luminosities of our Simulations

Dimension	Model	Box Size (cm)	Resolution	FW10%M (hour)	Peak Luminosity (10^{46} erg s $^{-1}$)
(1)	(2)	(3)	(4)	(5)	(6)
1D	N*	10^{14}	102400	0.153	6.1
	N	10^{14}	102400	0.174	2.9
2D	T	10^{14}	1024^2	1.54 ± 0.07	2.7 ± 0.4
	P*	10^{14}	1024^2	1.08 ± 0.22	1.7 ± 0.2
	P	10^{14}	1024^2	0.93 ± 0.12	4.1 ± 1.3
	R	10^{14}	1024^2	0.76 ± 0.06	4.8 ± 0.8
	B	4×10^{13}	2048^2	0.84 ± 0.09	2.97 ± 1.22

NOTE—We list the mean shock breakout duration and peak luminosity with standard deviation across viewing angles of our models calculated using the dominant band VIII during the shock breakout. The model setting can be found in Table 2. For 1D simulation, N is consistent with the previous 1D simulation (Lovegrove et al. 2017). The α in N* and P* are 0.5 and 5.0, respectively. Comparisons between models are discussed in §7.

of the companion star and the mixing regions. The envelope is heated by absorbing high energy radiation flux. For example, around 1.25 hours in Figure 22, we observe the luminosity drop in band VIII and the secondary luminosity spikes among bands IV to VII.

The companion star continues to stir the system, resulting in a faster luminosity drop rate of $\dot{L} = 4.5$ mag hour $^{-1}$ after 0.8 hours of the breakout peak luminosity. For band V, the luminosity increases with $\dot{L} = -1$ mag hour $^{-1}$. If the simulation continues, the highest energy band will shift to band V at around 2.5 hours because the expansion of the photosphere cools down radiation temperature, similar to the previous runs.

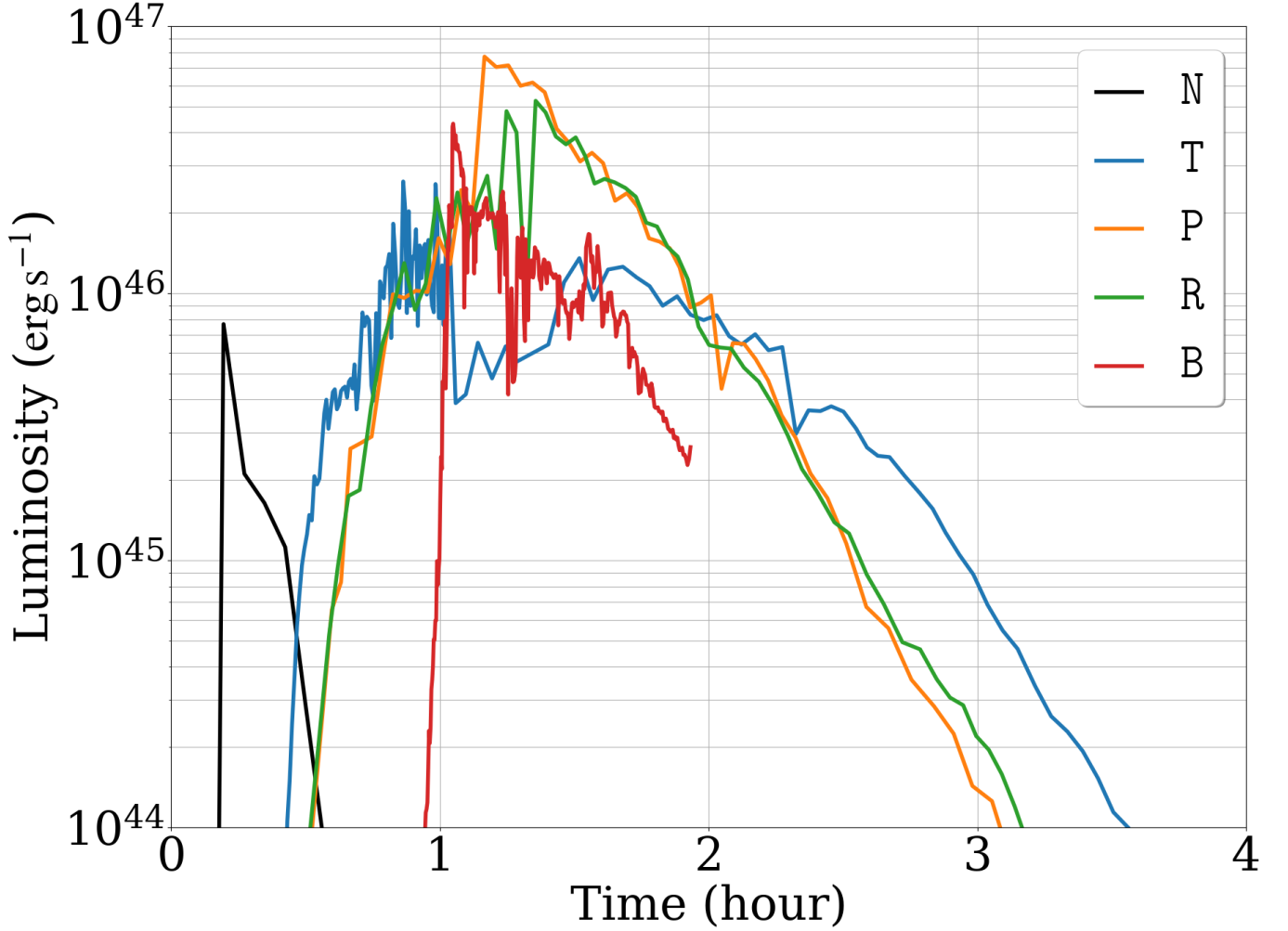


Figure 23. Comparison of band VIII LCs of 1D and four sets of 2D simulations with different CSM environments, the naming follows that of Table 2. 2D LCs look very different from the 1D simulation (N) in terms of duration and peak luminosity. 2D LCs are more realistic because the thin shell problem in 1D is satisfactorily solved. Comparing T with other models, the perturbed simulation (P) has a higher luminosity peak, and the simulation with a ring-like CSM (R) has a significant luminosity drop and presents stronger fluctuations before the breakout phase due to the radiation precursor interaction with the ring. Due to smaller box size, we compensate light travel time ~ 1580 s for the simulation with a binary companion (B).

7. DISCUSSION

7.1. Multi-Dimensional Effect

To evaluate the impact of perturbations and the different CSM environments on the shock breakout of SN 1987A progenitor, we compare all cases of LCs from our simulations in Figure 23 and summarize their characteristics in Table 3. We find that LCs from our multidimensional simulations have a longer duration than those in the previous 1D calculations (Ensmann & Burrows 1992; Matzner & McKee 1999; Lovegrove et al. 2017, for a consistent comparison, we estimate the shock breakout durations with our definition; we fit the luminosity variation rate if the data for 10% peak luminosity is unavailable). Previous 1D simulations are known for forming nonphysical thin shells near the forward shock due to limited degrees of freedom and inefficient relaxation of fluid instabilities, constraining the shock breakout duration.

Our shock breakout durations of ~ 1 hour agree well with the results from 2D ray-tracing calculations (Suzuki et al. 2016). Compared with previous 1D models, our 2D shock breakout durations are five times longer, and the peak luminosities are up to ten times brighter. This difference is attributed to the dimensional effect that shock can propagate in both r and z directions, mitigating the nonphysical thin shell found in 1D.

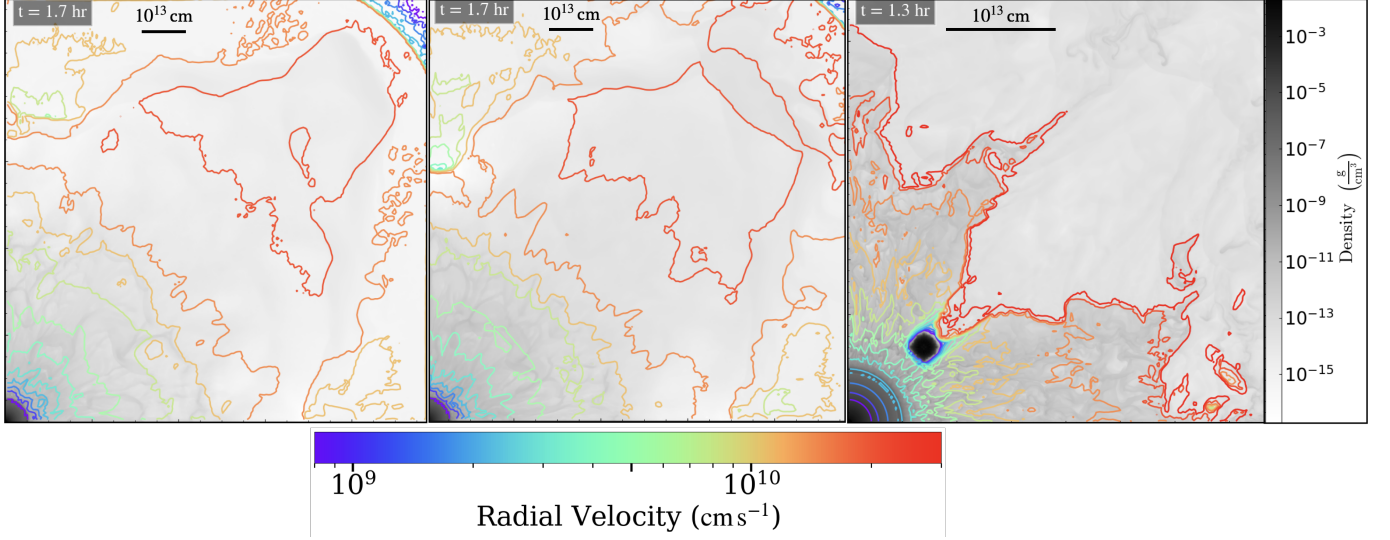


Figure 24. Snapshots of density and velocity of three scenarios at the end of simulations. From left to right are the breakout with steady wind CSM with perturbation (P), ring-like CSM (R), and explosion with a companion star (B), respectively. The distinct differences in the density and velocity distributions among the three models reflect the impact of the CSM on the shock breakout dynamics that affect the consequent observational signatures.

In contrast to 1D calculations with a spherical explosion environment, multidimensional simulations reflect the nature of radiation transport involving multi-wavelength radiation fluxes from various distances and angles (Chandrasekhar 2013, Page 13, Equation (71)). Multi-dimensional simulations account for the development of turbulent structures, breaking the spherical symmetry and enhancing fluid mixing. The formation of turbulence structures is sensitive to the progenitor star and its CSM profile, as shown in our multidimensional simulations.

Our simulations are more realistic than previous models because we consider the multidimensional and multi-group radiation hydrodynamics with detailed opacity. In Figure 24, the comparison of the development of turbulent structures under different CSM conditions is presented to remind readers of the impacts.

We list the shock breakout duration and peak luminosity for different 2D models (T, P, R, and B) in Table 3. Compared to T, inhomogeneities tend to shorten the shock breakout durations and increase the peak luminosities due to stronger mixing and asymmetry, which allows photons to escape more efficiently, the deviations in these models are also higher. While the shock breakout duration and peak luminosity with standard deviations on band VIII LCs reflect certain structures and asymmetries, comparing LCs across frequencies is also crucial for distinguishing between the models. We discuss detailed comparisons of these models in the following subsections.

7.1.1. Impact of perturbations

In §4, we contrast simulations with perturbations in a steady wind CSM (P) against test simulation (T). Comparing the LCs of P and T, R, and B in Figure 23, we find a higher peak luminosity, a longer shock breakout duration, and a stronger post-breakout mixing in Model P.

The initial small perturbations grow into a stronger mixing when the reverse shock develops via the deceleration of the forward shock. The perturbation stimulates turbulence behind the shock front structure and retards the shock propagation with stronger mixing. The LCs of the P shown in Figure 10 and Figure 12 exhibit small fluctuations across viewing angles during the rising phase. This suggests the pre-breakout emission is less affected by the perturbations. However, when the shock is about to breakout, where the opacity around the stellar surface decreases rapidly, mixing starts to impact the shock front. It results in large fluctuations in LCs across viewing angles. As we present in §4, the perturbation amplitude may affect the characteristics of shock breakout, which are closely related to the convective atmosphere formed during the late-time stellar evolution of massive stars. 2D MGFLD with the OPAL table successfully models the propagation of shock and the color evolution of LCs in such an environment.

7.1.2. Ring-Like CSM

We proceed to compare the results of shock breakout with (R) and without the ring-like CSM structure in Figure 23 and the middle panel of Figure 24. Comparing the LCs of R with T, we find a longer shock breakout duration, a higher

peak luminosity, and larger fluctuations prior to the peak in R. Although the shock structures of R and T are similar during the rising phase, the radiation precursor interacts with the ring earlier and leads to luminosity fluctuations and longer-wavelength luminosity bumps in Figure 16 and Figure 17.

When the shock collides with the ring-like CSM in the middle panel of Figure 14, it creates the impinging flows around the ring-like CSM. The asymmetric geometry formed by the shock collision creates gaps for radiation to escape from the emission layer that extend the shock breakout duration and boost the peak luminosity. The ring-like CSM absorbs radiation energy into longer wavelengths, as seen in the sudden drop in Figure 17 and slows down the shock propagation. The post-breakout plateau phase in T is replaced with a luminosity decline rate slightly slower than that of Model P.

7.1.3. Explosion with a Companion Star

We now compare the explosion with a nearby companion star (B) to other 2D simulations (P, T, and R) in Figure 23 and the right panel of Figure 24. Compared to the T and P in Figure 23, the LC rising phase is shorter due to the destruction of the shock front by the blocking of the binary. The surviving binary companion continues to create larger fluctuation in LCs across viewing angles after breakout than the contribution from the mixing of the ring in R. The longer frequency shows clear double-peak LCs, which are a unique feature (see discussion in Kasen et al. 2016). Depending on the nature of the companion star, such as a red or blue supergiant, the emission from the surviving companion during the breakout phase can vary.

To summarize multi-dimensional effects on our studies, the mixing in the post-breakout is sensitive to the physical properties of CSM and companion stars. Therefore, the breakout LCs also vary across viewing angles among all models. These effects are unavailable in previous 1D calculations. Furthermore, our MGFLD with realistic opacity can provide the color evolution of the LC that probes the nature of the pre-supernova environment.

7.2. Further Improvements and Limitations

7.2.1. Observational Perspective

Although shock breakout of SN 1987A had not been directly detected, we can probe the early phase from the UV observations of SN 1987A around 1 day after the event (Cassatella et al. 1987; Ensmann & Burrows 1992), when the radiation temperature has cooled to around 14,000 K and continued dropping to around 10,000 K after another 24 hours. Based on our simulations, the radiation temperature reaches $\sim 10^7$ K right after the breakout, and the luminosity reaches its peak following a luminosity decay rate of $\sim 1.5 \text{ mag hour}^{-1}$. The color evolution also agrees well with the observational data of 1987A. (Singh et al. 2019; Fransson & Lundqvist 1989)

Searching the early emission of SN shock breakouts is more approachable with X-ray and UV observations (Predehl, P. et al. 2021; Kozyreva et al. 2020; Bayless et al. 2022) corresponding to the band V to band VIII in our simulation. The late-time shock breakout emission can possibly be probed by the excessive optical and infrared rays (Dwek & Arendt 2008; Suwa 2017) falling in the bands I to IV in our simulations. Furthermore, shock breakouts characterized by a sharp luminosity transition within short time periods is more suitable for high redshift observations and can provide promising clues of the evolution of the early universe (Blondin et al. 2008).

7.2.2. Realistic Opacity

We use opacities derived from the OPAL table depending on the gas density, temperature, and radiation frequency. Our simulations properly model the post-breakout cooling and produce correct color LCs with a rapid luminosity decline rate that cannot be done with a constant opacity. However, this opacity can be further improved by using multiple opacity tables from Seaton (2005); Poutanen (2017) for gas temperature $\geq 10^4$ K, and Ferguson et al. (2005); Marigo & Aringer (2009) for gas temperature $< 10^4$ K. These tables are operated well in the MESA code (Paxton et al. 2011, 2013, 2015, 2018, 2019; Jermyn et al. 2023) that cover wider range of density, temperature, and metallicity, especially taking into account individual line opacities contributed from ^{56}Ni , carbon, and oxygen. Although the total opacity may not change dramatically, it may reflect in line emissions and absorption of SN spectra.

7.2.3. Towards 3D Simulations

In this study, we only show the results from 2D simulation. However, the 3D can be more realistic than 2D due to the nature of turbulence. 3D simulation allows (r, θ, ϕ) motions that can further break cylindrical symmetry (Goldberg et al. 2022). High-velocity bulbs in 2D explosion shock seen in Figure 8, Figure 14, and Figure 18 may evolve into 3D

bubbles with Rayleigh-Bénard convection that the radiative heating post-shocked regions mix with radiative cooling shock front. Nevertheless, our 2D simulations generally have an advantage in following later evolution with higher resolution. Furthermore, stellar convection and its penetration depth show no significant difference in the stellar simulations between 2D and 3D (Pratt et al. 2020).

7.2.4. Realistic Circumstellar Medium

We examine different CSM structures by adjusting the α parameter for mass loss rates of the steady wind and placing a ring-like structure. In reality, CSMs reflect time-dependent mass loss history of the progenitor stars (Bayless et al. 2015), and the bipolar or disk-like geometry is needed to explain some SN LCs (Chandra 2018; Irwin et al. 2021). The internal motion of CSM may also affect the shock breakout dynamics and its LC. Our simulation results can be used as input for post-processing the spectra of SN 1987A.

8. CONCLUSIONS

We perform the first 2D MGFLD simulations of the shock breakout of SN 1987A with realistic opacities using the OPAL table. 2D Mixing in the gas decodes the nonphysical thin shell found in previous 1D models and allows us to study nonuniform pre-supernova environments such as stellar convection, eruptive mass loss wind, and a binary companion. Our multi-group radiation hydrodynamics simulations count eight radiation bands ranging from X-ray to infrared that offer the color evolution of shock breakout emissions and unveil the impact of radiative cooling on the shock propagation.

We find that the shock breakout durations of ~ 1 hour observed in our simulation results agree well with the previous study (Suzuki et al. 2016). The dominant bands ranging from X-ray to UV due to the expansion of the photosphere offer clues for the observational strategy for shock breakouts. Moreover, we discovered that the radiation precursor interaction with a ring-like CSM can lead to substantial fluctuations and that double-peaked X-ray LCs could occur in the case with a binary companion. We plan to advance this study with more realistic opacities, including line emission and absorption in 3D geometry. Furthermore, we will explore the shock breakouts of RSG and BSG progenitors with asymmetric explosion mechanisms.

Our 2D MGFLD simulations of the SN 1987A shock breakout demonstrate the impact of the pre-breakout environments and the opacity on the emission and dynamics of the shock propagation. This work can extend to provide solid predictions for future searches of SN shock breakouts and deepen our understanding of the physics of supernovae and their exploding environments.

¹ We thank Po-Sheng Ou and Sung-Han Tsai for the useful discussion. This research is supported by the National Science
² and Technology Council, Taiwan under grant no. MOST 110-2112-M-001-068-MY3 and the Academia Sinica, Taiwan
³ under a career development award under grant no. AS-CDA-111-M04. Our computing resources were supported by
⁴ the National Energy Research Scientific Computing Center (NERSC), a U.S. Department of Energy Office of Science
⁵ User Facility operated under Contract No. DE-AC02-05CH11231, and the TIARA Cluster at the Academia Sinica
⁶ Institute of Astronomy and Astrophysics (ASIAA).

REFERENCES

- | | |
|--|---|
| <p>Almgren, A., Sazo, M. B., Bell, J., et al. 2020, Journal of Open Source Software, 5, 2513, doi: 10.21105/joss.02513</p> <p>Almgren, A. S., Beckner, V. E., Bell, J. B., et al. 2010, ApJ, 715, 1221, doi: 10.1088/0004-637X/715/2/1221</p> <p>Alp, D., Larsson, J., Maeda, K., et al. 2019, ApJ, 882, 22, doi: 10.3847/1538-4357/ab3395</p> <p>Arnett, W. D., Bahcall, J. N., Kirshner, R. P., & Woosley, S. E. 1989, <i>Yaraa</i>, 27, 629, doi: 10.1146/annurev.aa.27.090189.003213</p> <p>Bayless, A. J., Even, W., Frey, L. H., et al. 2015, ApJ, 805, 98, doi: 10.1088/0004-637X/805/2/98</p> | <p>Bayless, A. J., Fryer, C., Brown, P. J., et al. 2022, The Astrophysical Journal, 931, 15, doi: 10.3847/1538-4357/ac674c</p> <p>Blondin, S., Davis, T. M., Krisciunas, K., et al. 2008, The Astrophysical Journal, 682, 724, doi: 10.1086/589568</p> <p>Buchler, J. R., & Yueh, W. R. 1976, ApJ, 210, 440, doi: 10.1086/154847</p> <p>Cassatella, A., Fransson, C., van Santvoort, J., et al. 1987, A&A, 177, L29</p> <p>Chandra, P. 2018, SSRv, 214, 27, doi: 10.1007/s11214-017-0461-6</p> |
|--|---|

- Chandrasekhar, S. 2013, *Radiative Transfer*, Dover Books on Physics (Dover Publications). <https://books.google.com.tw/books?id=1YHCAGAAQBAJ>
- Chen, K.-J., Heger, A., & Almgren, A. S. 2013, *Astronomy and Computing*, 3-4, 70, doi: <https://doi.org/10.1016/j.ascom.2014.01.001>
- Chen, K.-J., Heger, A., Woosley, S., Almgren, A., & Whalen, D. J. 2014, *ApJ*, 792, 44, doi: [10.1088/0004-637X/792/1/44](https://doi.org/10.1088/0004-637X/792/1/44)
- Chen, K.-J., Whalen, D. J., Woosley, S. E., & Zhang, W. 2023, *ApJ*, 955, 39, doi: [10.3847/1538-4357/ace968](https://doi.org/10.3847/1538-4357/ace968)
- Chevalier, R. A., & Fransson, C. 1987, *Nature*, 328, 44, doi: [10.1038/328044a0](https://doi.org/10.1038/328044a0)
- Chevalier, R. A., & Irwin, C. M. 2011, *ApJL*, 729, L6, doi: [10.1088/2041-8205/729/1/L6](https://doi.org/10.1088/2041-8205/729/1/L6)
- Couch, S. M., Pooley, D., Wheeler, J. C., & Milosavljević, M. 2011, *ApJ*, 727, 104, doi: [10.1088/0004-637X/727/2/104](https://doi.org/10.1088/0004-637X/727/2/104)
- Dohi, A., Greco, E., Nagataki, S., et al. 2023, *ApJ*, 949, 97, doi: [10.3847/1538-4357/acce3f](https://doi.org/10.3847/1538-4357/acce3f)
- Dwek, E., & Arendt, R. G. 2008, *The Astrophysical Journal*, 685, 976, doi: [10.1086/589988](https://doi.org/10.1086/589988)
- Ensmann, L., & Burrows, A. 1992, *ApJ*, 393, 742, doi: [10.1086/171542](https://doi.org/10.1086/171542)
- Epstein, R. I. 1981, *ApJL*, 244, L89, doi: [10.1086/183486](https://doi.org/10.1086/183486)
- Ferguson, J. W., Alexander, D. R., Allard, F., et al. 2005, *ApJ*, 623, 585, doi: [10.1086/428642](https://doi.org/10.1086/428642)
- Fransson, C., & Lundqvist, P. 1989, *ApJL*, 341, L59, doi: [10.1086/185457](https://doi.org/10.1086/185457)
- Förster, F., Moriya, T., Maureira, J., et al. 2018, *Nature Astronomy*, 2, doi: [10.1038/s41550-018-0563-4](https://doi.org/10.1038/s41550-018-0563-4)
- Gezari, S., Jones, D. O., Sanders, N. E., et al. 2015, *ApJ*, 804, 28, doi: [10.1088/0004-637X/804/1/28](https://doi.org/10.1088/0004-637X/804/1/28)
- Goldberg, J. A., Jiang, Y.-F., & Bildsten, L. 2022, *ApJ*, 933, 164, doi: [10.3847/1538-4357/ac75e3](https://doi.org/10.3847/1538-4357/ac75e3)
- González-Torà, G., Wittkowski, M., Davies, B., Plez, B., & Kravchenko, K. 2023, *A&A*, 669, A76, doi: [10.1051/0004-6361/202244503](https://doi.org/10.1051/0004-6361/202244503)
- Greco, E., Miceli, M., Orlando, S., et al. 2021, *ApJL*, 908, L45, doi: [10.3847/2041-8213/abdf5a](https://doi.org/10.3847/2041-8213/abdf5a)
- . 2022, *ApJ*, 931, 132, doi: [10.3847/1538-4357/ac679d](https://doi.org/10.3847/1538-4357/ac679d)
- Iglesias, C. A., & Rogers, F. J. 1996, *ApJ*, 464, 943, doi: [10.1086/177381](https://doi.org/10.1086/177381)
- Imshennik, V. S., & Nadezhin, D. K. 1988, *Soviet Astronomy Letters*, 14, 449
- Irwin, C. M., Linial, I., Nakar, E., Piran, T., & Sari, R. 2021, *MNRAS*, 508, 5766, doi: [10.1093/mnras/stab2705](https://doi.org/10.1093/mnras/stab2705)
- Jermyn, A. S., Bauer, E. B., Schwab, J., et al. 2023, *ApJS*, 265, 15, doi: [10.3847/1538-4365/aca8d](https://doi.org/10.3847/1538-4365/aca8d)
- Kasen, D., Metzger, B. D., & Bildsten, L. 2016, *ApJ*, 821, 36, doi: [10.3847/0004-637X/821/1/36](https://doi.org/10.3847/0004-637X/821/1/36)
- Katz, B., Budnik, R., & Waxman, E. 2010, *The Astrophysical Journal*, 716, 781, doi: [10.1088/0004-637X/716/1/781](https://doi.org/10.1088/0004-637X/716/1/781)
- Katz, M. P., Zingale, M., Calder, A. C., et al. 2016, *ApJ*, 819, 94, doi: [10.3847/0004-637X/819/2/94](https://doi.org/10.3847/0004-637X/819/2/94)
- Kozyreva, A., Nakar, E., Waldman, R., Blinnikov, S., & Baklanov, P. 2020, *MNRAS*, 494, 3927, doi: [10.1093/mnras/staa924](https://doi.org/10.1093/mnras/staa924)
- Leung, S.-C., Wu, S., & Fuller, J. 2021, *ApJ*, 923, 41, doi: [10.3847/1538-4357/ac2c63](https://doi.org/10.3847/1538-4357/ac2c63)
- Levesque, E., Stringfellow, G., Ginsburg, A., Bally, J., & Keeney, B. 2012, *The Astronomical Journal*, 147, doi: [10.1088/0004-6256/147/1/23](https://doi.org/10.1088/0004-6256/147/1/23)
- Levinson, A., & Nakar, E. 2020, *Physics Reports*, 866, 1, doi: <https://doi.org/10.1016/j.physrep.2020.04.003>
- Lovegrove, E., Woosley, S. E., & Zhang, W. 2017, *ApJ*, 845, 103, doi: [10.3847/1538-4357/aa7b7d](https://doi.org/10.3847/1538-4357/aa7b7d)
- Mao, J., Ono, M., Nagataki, S., et al. 2015, *The Astrophysical Journal*, 808, 164, doi: [10.1088/0004-637X/808/2/164](https://doi.org/10.1088/0004-637X/808/2/164)
- Marigo, P., & Aringer, B. 2009, *A&A*, 508, 1539, doi: [10.1051/0004-6361/200912598](https://doi.org/10.1051/0004-6361/200912598)
- Matzner, C. D., & McKee, C. F. 1999, *ApJ*, 510, 379, doi: [10.1086/306571](https://doi.org/10.1086/306571)
- Menon, A., & Heger, A. 2017, *MNRAS*, 469, 4649, <https://arxiv.org/abs/1703.04918>
- Menon, A., Utrobin, V., & Heger, A. 2019, *MNRAS*, 482, 438, doi: [10.1093/mnras/sty2647](https://doi.org/10.1093/mnras/sty2647)
- Nakamura, K., Takiwaki, T., & Kotake, K. 2022, *MNRAS*, 514, 3941, doi: [10.1093/mnras/stac1586](https://doi.org/10.1093/mnras/stac1586)
- Ono, M., Nagataki, S., Ferrand, G., et al. 2020, *ApJ*, 888, 111, doi: [10.3847/1538-4357/ab5dba](https://doi.org/10.3847/1538-4357/ab5dba)
- Ono, M., Nozawa, T., Nagataki, S., et al. 2023, *arXiv e-prints*, arXiv:2305.02550, doi: [10.48550/arXiv.2305.02550](https://doi.org/10.48550/arXiv.2305.02550)
- Orlando, S., Ono, M., Nagataki, S., et al. 2020, *A&A*, 636, A22, doi: [10.1051/0004-6361/201936718](https://doi.org/10.1051/0004-6361/201936718)
- Ott, C. D., Burrows, A., Dessart, L., & Livne, E. 2008, *The Astrophysical Journal*, 685, 1069, doi: [10.1086/591440](https://doi.org/10.1086/591440)
- Paxton, B., Bildsten, L., Dotter, A., et al. 2011, *ApJS*, 192, 3, doi: [10.1088/0067-0049/192/1/3](https://doi.org/10.1088/0067-0049/192/1/3)
- Paxton, B., Cantiello, M., Arras, P., et al. 2013, *ApJS*, 208, 4, doi: [10.1088/0067-0049/208/1/4](https://doi.org/10.1088/0067-0049/208/1/4)
- Paxton, B., Marchant, P., Schwab, J., et al. 2015, *ApJS*, 220, 15, doi: [10.1088/0067-0049/220/1/15](https://doi.org/10.1088/0067-0049/220/1/15)
- Paxton, B., Schwab, J., Bauer, E. B., et al. 2018, *ApJS*, 234, 34, doi: [10.3847/1538-4365/aaa5a8](https://doi.org/10.3847/1538-4365/aaa5a8)

- Paxton, B., Smolec, R., Schwab, J., et al. 2019, *ApJS*, 243, 10, doi: [10.3847/1538-4365/ab2241](https://doi.org/10.3847/1538-4365/ab2241)
- Podsiadlowski, P. 2017, *The Progenitor of SN 1987A*, ed. A. W. Alsabti & P. Murdin (Cham: Springer International Publishing), 1–14, doi: [10.1007/978-3-319-20794-0_123-1](https://doi.org/10.1007/978-3-319-20794-0_123-1)
- Poutanen, J. 2017, *ApJ*, 835, 119, doi: [10.3847/1538-4357/835/2/119](https://doi.org/10.3847/1538-4357/835/2/119)
- Pratt, J., Baraffe, I., Goffrey, T., et al. 2020, *A&A*, 638, A15, doi: [10.1051/0004-6361/201834736](https://doi.org/10.1051/0004-6361/201834736)
- Predehl, P., Andritschke, R., Arefiev, V., et al. 2021, *A&A*, 647, A1, doi: [10.1051/0004-6361/202039313](https://doi.org/10.1051/0004-6361/202039313)
- Sapienza, V., Miceli, M., Bamba, A., et al. 2024, *ApJL*, 961, L9, doi: [10.3847/2041-8213/ad16e3](https://doi.org/10.3847/2041-8213/ad16e3)
- Schawinski, K., Justham, S., Wolf, C., et al. 2008, *Science*, 321, 223, doi: [10.1126/science.1160456](https://doi.org/10.1126/science.1160456)
- Seaton, M. J. 2005, *MNRAS*, 362, L1, doi: [10.1111/j.1365-2966.2005.00019.x](https://doi.org/10.1111/j.1365-2966.2005.00019.x)
- Sharma, V. D., Ram, R., & Sachdev, P. L. 1987, *Journal of Fluid Mechanics*, 185, 153–170, doi: [10.1017/S0022112087003124](https://doi.org/10.1017/S0022112087003124)
- Singh, A., Sahu, D. K., Anupama, G. C., et al. 2019, *ApJL*, 882, L15, doi: [10.3847/2041-8213/ab3d44](https://doi.org/10.3847/2041-8213/ab3d44)
- Sugerman, B. E. K., Crotts, A. P. S., Kunkel, W. E., Heathcote, S. R., & Lawrence, S. S. 2005, *ApJ*, 627, 888, doi: [10.1086/430396](https://doi.org/10.1086/430396)
- Suwa, Y. 2017, *Monthly Notices of the Royal Astronomical Society*, 474, 2612, doi: [10.1093/mnras/stx2953](https://doi.org/10.1093/mnras/stx2953)
- Suzuki, A., & Maeda, K. 2021, *ApJ*, 908, 217, doi: [10.3847/1538-4357/abd54c](https://doi.org/10.3847/1538-4357/abd54c)
- Suzuki, A., Maeda, K., & Shigeyama, T. 2016, *Astrophysical Journal*, 825, doi: [10.3847/0004-637X/825/2/92](https://doi.org/10.3847/0004-637X/825/2/92)
- Tolstov, A. G., Blinnikov, S. I., & Nadyozhin, D. K. 2013, *Monthly Notices of the Royal Astronomical Society*, 429, 3181, doi: [10.1093/mnras/sts577](https://doi.org/10.1093/mnras/sts577)
- Tsai, S.-H., Chen, K.-J., Whalen, D., Ou, P.-S., & Woods, T. E. 2023, *The Astrophysical Journal*, 951, 84, doi: [10.3847/1538-4357/acd936](https://doi.org/10.3847/1538-4357/acd936)
- Urushibata, T., Takahashi, K., Umeda, H., & Yoshida, T. 2018, *MNRAS*, 473, L101, doi: [10.1093/mnrasl/slx166](https://doi.org/10.1093/mnrasl/slx166)
- Utrobin, V. P., Wongwathanarat, A., Janka, H. T., et al. 2021, *ApJ*, 914, 4, doi: [10.3847/1538-4357/abf4c5](https://doi.org/10.3847/1538-4357/abf4c5)
- Walborn, N. R., Lasker, B. M., Laidler, V. G., & Chu, Y.-H. 1987, *ApJL*, 321, L41, doi: [10.1086/185002](https://doi.org/10.1086/185002)
- Waxman, E., & Katz, B. 2017, in *Handbook of Supernovae*, ed. A. W. Alsabti & P. Murdin (Springer, Cham), 967, doi: [10.1007/978-3-319-21846-5_33](https://doi.org/10.1007/978-3-319-21846-5_33)
- Weaver, T. A., Zimmerman, G. B., & Woosley, S. E. 1978, *ApJ*, 225, 1021, doi: [10.1086/156569](https://doi.org/10.1086/156569)
- West, R. M., Lauberts, A., Jorgensen, H. E., & Schuster, H. E. 1987, *A&A*, 177, L1
- Wheeler, J. C., Lecar, M., & McKee, C. F. 1975, *ApJ*, 200, 145, doi: [10.1086/153771](https://doi.org/10.1086/153771)
- Woosley, S. E., Blinnikov, S., & Heger, A. 2007, *Nature*, 450, 390, doi: [10.1038/nature06333](https://doi.org/10.1038/nature06333)
- Yamaguchi, H., Acero, F., Li, C.-J., & Chu, Y.-H. 2021, *The Astrophysical Journal Letters*, 910, L24, doi: [10.3847/2041-8213/abee8a](https://doi.org/10.3847/2041-8213/abee8a)
- Zhang, W., Howell, L., Almgren, A., Burrows, A., & Bell, J. 2011, *ApJS*, 196, 20, doi: [10.1088/0067-0049/196/2/20](https://doi.org/10.1088/0067-0049/196/2/20)
- Zhang, W., Howell, L., Almgren, A., et al. 2013, *ApJS*, 204, 7, doi: [10.1088/0067-0049/204/1/7](https://doi.org/10.1088/0067-0049/204/1/7)